RUPRECHT-KARLS-UNIVERSITÄT HEIDELBERG

Henning Flächer

Study of Dimuon pair production in e^+e^- collisions from 196 - 202 GeV

Diplomarbeit

HD-KIP-00-24

KIRCHHOFF-INSTITUT FÜR PHYSIK

Fakultät für Physik und Astronomie
Ruprecht-Karls-Universität Heidelberg

HD-KIP-00-24

Diplomarbeit
im Studiengang Physik

vorgelegt von
Henning Flächer
aus Sinsheim
Juli 2000

Study of Dimuon pair production in e^+e^- collisions from 196 - 202 GeV

Die Diplomarbeit wurde von Henning Flächer ausgeführt am
Kirchhoff-Institut für Physik
unter der Betreuung von
Prof. Dr. Alois Putzer

Abstract

In this thesis the electroweak process $e^+e^- \to \mu^+\mu^-$ was studied and an inclusive and exclusive cross section were measured. Furthermore the forward-backward asymmetry A_{FB} was determined from the exclusive event sample. The investigated data was recorded with the detector ALEPH at centre-of-mass energies of 196, 200 and 202 GeV resulting in a total integrated luminosity of 208.1 pb^{-1}. All the measured results are in good agreement with the Standard Model.
From the measurements of total cross sections and angular distributions for all the two fermion processes at energies from 130 - 202 GeV limits on processes beyond the Standard Model were derived. For Contact Interactions they were found to be of the order of 10 TeV while for TeV-Scale Quantum Gravity a limit for the ultra-violet cut-off parameter of $\Lambda \approx 1$ TeV could be derived.

Zusammenfassung

In dieser Diplomarbeit wurde ein inklusiver und exklusiver Wirkungsquerschnitt für den elektroschwachen Prozess $e^+e^- \to \mu^+\mu^-$ gemessen. Darüberhinaus wurde für die exklusive Messung die Vorwärts-Rückwärts-Asymmetrie A_{FB} bestimmt. Die untersuchten Daten wurden mit dem Detektor ALEPH bei Schwerpunktenergien von 196, 200 und 202 GeV aufgezeichnet. Die Gesamtluminosität beträgt 208.1 pb^{-1}. Die Ergebnisse der Messungen stimmen gut mit dem Standardmodell überein.
Aus den Winkelverteilungen und Wirkungsquerschnittsmessungen für alle Zwei-Fermion Prozesse die bei Energien von 130 - 202 GeV bestimmt wurden, konnten Grenzwerte für physikalische Prozesse jenseits des Standardmodells abgeleitet werden. Für Kontaktwechselwirkungen wurde eine Energieskala von ungefähr 10 TeV bestimmt. Für das Modell der Quantengravitation im TeV-Bereich konnte für den ultravioletten Abschneideparameter Λ ein Wert von ca. 1 TeV abgeleitet werden.

Contents

1 Introduction 1

2 Theoretical Framework 5
- 2.1 Electroweak Physics . . . 5
  - 2.1.1 Electroweak Unification . . . 5
  - 2.1.2 The Process $e^+e^- \to \mu^+\mu^-$ . . . 7
  - 2.1.3 Radiative Corrections . . . 8
- 2.2 Definitions of Cross Sections and Asymmetry . . . 8
- 2.3 Physics Beyond the Standard Model . . . 11

3 The ALEPH Experiment at LEP 13
- 3.1 LEP Collider . . . 13
- 3.2 ALEPH Detector . . . 14
  - 3.2.1 Tracking Detectors . . . 15
  - 3.2.2 Calorimeters . . . 16

4 Event Selection 19
- 4.1 Muon Identification . . . 19
- 4.2 Dimuon Selection . . . 21
- 4.3 Acceptance and Efficiency . . . 21
- 4.4 Background Estimation . . . 24
  - 4.4.1 Background from two-photon exchange events . . . 25
  - 4.4.2 Background from other processes . . . 25
  - 4.4.3 Double Radiative Events . . . 27

5 Dimuon Cross-Section and A_{FB} 29
- 5.1 Cross Section Measurement . . . 29
- 5.2 Measurement of the Dimuon Asymmetry . . . 33
- 5.3 Systematic Errors and Corrections . . . 37

6 New Physics 43
- 6.1 Limits on Four Fermion Contact Interactions . . . 43
- 6.2 Limits on TeV-Scale Quantum Gravity . . . 48

7 Conclusions and Comparisons 53

A Formulae and Functions for New Physics **57**
A.1 Born level differential cross section for Contact Interactions 57
A.2 The $G_i(x)$ functions for TeV Scale Quantum Gravity 58

Chapter 1

Introduction

> The beginning is the most important part of the work.
>
> Plato

The aim of modern particle physics is to describe the constituents of matter and the interactions between them with a self-consistent, single theory. In order to achieve this aim, physicists are investigating the properties of matter at smaller and smaller scales. To our present knowledge there are two types of point-like particles, fermions and bosons. The former are spin-$\frac{1}{2}$ particles obeying Fermi-Dirac statistics, which means that two particles of the same kind cannot be in the same quantum state simultaneously. All solid matter is built up of fermions, which themselves can be divided into two groups - quarks and leptons. The bosons are particles with integral spin, following Bose-Einstein statistics, which means that more than one particle can be in the same quantum state at the same time and they mediate the interaction forces between quarks and leptons.

To today's knowledge there are four fundamental forces: the electromagnetic, the weak, the strong and the gravitational force. The photons are the carriers of the electromagnetic force, the weak force is mediated by the $W^{\pm}$ and Z bosons while the strong force is carried by eight gluons. The graviton, responsible for the gravitational force, differs from the other force-carriers as it is assumed to be a spin-2 particle in contrast to the photon, $W^{\pm}$, Z and gluons which have spin 1.

According to the current theory, called the Standard Model (SM) of particle physics, left-handed leptons as well as quarks appear as doublets of the weak isospin while the righthanded fermions only appear as singlets. Both come in three families or generations that only differ in their masses. The charged leptons participate in the electromagnetic and the weak interactions while the neutral leptons (neutrinos) are only subject to the weak force. The three pairs of quarks are subject to all interactions and exist in three different colour states. Furthermore, all fermions have corresponding antiparticles.

Each of the four forces has different strength, which is expressed in their respective couplings. Although all massive particles experience the gravitational force, it is by far the weakest. The other three coupling constants are of the same order of magnitude and vary with the energy scale at which the corresponding phenomena are investigated.

A first great success to the understanding of particle interactions was the development of Quantum Electro-Dynamics (QED), the theory of electromagnetic interactions which achieved to combine quantum mechanics with special relativity. It was developed to a great part by Dyson, Feynman, Schwinger and Tomonaga and a review of the evolution of the theory can be found in [1]. The probably most important feature of this theory is that it remains renormalizable through the requirement of local gauge invariance, even when considering higher order processes. Due to the success of QED for all electromagnetic phenomena, local gauge invariance is regarded as a fundamental property for any future theory that tries to combine or unify two or more of the fundamental forces described above.

The unification of electromagnetism and the weak force in an electroweak theory then followed this approach but some problems emerged as theories based on local gauge invariance required massless gauge bosons while the apparently point-like nature of weak interactions required a very massive exchange particle to account for the very short range over which it acts. Thanks to the Higgs mechanism [2, 3, 4], invented by P. W. Higgs, this problem could be solved by breaking the underlying gauge symmetries at low energies. Still, there was one problem left: The electroweak theory, developed by Glashow, Salam and Weinberg [5, 6, 7] predicted a neutral weak gauge boson (the Z) that had not been observed so far and all known weak interactions could be accounted for in terms of $W^{\pm}$ exchange. In addition, an extra scalar boson is predicted to exist, the Higgs boson.

In 1982 and 1983 the $W^{\pm}$ and Z were discovered by the UA1 [8, 9] and UA2 [10, 11] collaborations in $p\bar{p}$ collisions at the Super Antiproton-Proton Storage ring (S$\bar{\text{p}}$pS) at CERN[1]. With the observation of the three bosons and their predicted masses already several of the predictions of the electroweak theory had been verified. The only particle still waiting for discovery is the Higgs boson.

From 1989 to 1995 the LEP[2] collider at CERN ran at a centre-of-mass energy approximately equal to the Z mass resulting in a precise measurement of the cross section, mass and width of the neutral carrier of the weak force. In summer 1996 LEP ran at a centre-of-mass energy of about 161 GeV and was thus able to produce W pairs. From the behaviour of the cross section for this process the existence of triple gauge couplings could be confirmed.

Together with Quantum Chromo Dynamics (QCD), the theory describing strong interactions between quarks and gluons, the electroweak theory forms the SM. The couplings of the three forces are assumed to unify at a scale of $\sim 10^{15}$ GeV resulting in Grand Unified Theories (G.U.T.) while the energy scale at which gravity becomes as strong as the (then probably unified) remaining three forces is the Planck scale at $\sim 10^{19}$ GeV. The unification of the fundamental forces in nature remains the probably most challenging task in particle physics and in order to achieve this, several extensions to the SM have been developed.

In this diploma thesis the cross section and asymmetry for the process $e^+e^- \to \mu^+\mu^-$ at centre-of-mass energies of 196 GeV to 202 GeV are measured. The dimuon pair in the final state can be either produced by a virtual photon or Z. Cross section measurements are important as predictions of the electroweak theory can be verified. Additionally, the interference between the photon and the Z exchange leads to an asymmetric angular distribution that

[1] CERN: Conseil Européen pour la Recherche Nucléaire
[2] LEP: Large Electron Positron collider

reveals the structure of the couplings. From deviations between the measured and predicted cross sections and asymmetries limits on energy scales where physics processes arise that are extensions to the SM can be derived. For these reasons cross section and asymmetry measurements provide an interesting testing ground for the SM.

The outline of this thesis is as follows:
In chapter 2 a short introduction to electroweak physics is given with emphasis on dimuon production. Furthermore, cross sections and asymmetries are defined and experimental variables are introduced. Chapter 3 provides a description of the experimental apparatus, the LEP collider and the ALEPH[3] detector. In the next chapter the muon identification and event selection is described while chapter 5 is devoted to the cross section and asymmetry measurement as well as to the study of systematic errors. In chapter 6 limits on Contact Interactions and TeV-Scale Quantum Gravity are derived. The results of this analysis are compared with those of other experiments in the final conclusions in the last chapter.

[3]ALEPH: Apparatus for LEP PHysics

Chapter 2

Theoretical Framework

The purpose of this chapter is to provide a short introduction to the basic concepts of the electroweak theory. Detailed descriptions of the SM and its physics can be found in textbooks, e.g. [12, 13, 14]. Furthermore, the definitions of the cross sections and asymmetries that are measured in this analysis are given and the variables needed for these measurements are introduced. The notation follows [12] using the Dirac-Pauli representation.

2.1 Electroweak Physics

2.1.1 Electroweak Unification

When trying to unify the electromagnetic and the weak interaction one was looking for a renormalizable theory and therefore a theory with local gauge invariance (as in QED) had to be developed. The electroweak interaction is assumed to be invariant under transformations of the form

$$\psi \rightarrow \psi' = e^{i\frac{g'}{2}Y\alpha(x)} \cdot e^{ig\,\boldsymbol{\sigma}\boldsymbol{\Lambda}(x)}\,\psi \tag{2.1}$$

which correspond to an invariance under a local phase change $\alpha(x)$ and a local rotation of the weak isospin I about an axis $\boldsymbol{\Lambda}(x)$. g and g' are coupling constants, $\boldsymbol{\sigma}$ are the three Pauli spin matrices and Y is the weak hypercharge. The weak isospin I and the weak hypercharge Y are related to the electric charge Q (in units of e) through the formula[1]:

$$Q = I_3 + \frac{1}{2}Y \tag{2.2}$$

The gauge transformations in eq. 2.1 form elements of a group $U(1) \otimes SU(2)$ and in order to achieve that the Lagrangian remains invariant under these transformations, the covariant derivative has to be of the form:

$$D_\mu = \partial_\mu + i\frac{g'}{2}YB_\mu + ig\,\boldsymbol{\sigma}\boldsymbol{W}_\mu \qquad . \tag{2.3}$$

Thus the condition of local gauge invariance requires the introduction of four gauge bosons or gauge fields. A singlet, called B, coupling to the hypercharge Y and a triplet, W^1, W^2

[1] The weak isospin and weak hypercharge are introduced in analogy to the Gell-Mann - Nishijima scheme for the strong isospin multiplets.

and W^3, coupling to the three components of the weak isospin I. With these fields the $U(1) \otimes SU(2)$ invariant Lagrangian acquires the form

$$\begin{aligned} \mathcal{L} = \; & \sum_f \left[\bar{f}_L \gamma^\mu \left(i\partial_\mu - \tfrac{g'}{2} Y B_\mu - g \sigma_i W_\mu^i \right) f_L + \bar{f}_R \gamma^\mu \left(i\partial_\mu - \tfrac{g'}{2} Y B_\mu \right) f_R \right] \\ & - \tfrac{1}{4} W^i_{\mu\nu} W_i^{\mu\nu} - \tfrac{1}{4} B_{\mu\nu} B^{\mu\nu} \end{aligned} \tag{2.4}$$

where the sum is over all the left- and right-handed fermion fields, f_L and f_R. The last two terms in eq. 2.4 describe the kinetic energies and self-interactions of the gauge boson fields.

As a result of the spontaneous symmetry breaking induced by the Higgs mechanism [2, 3, 4] the four gauge bosons mix to form mass eigenstates:

$$\begin{aligned} W_\mu^\pm &= \frac{1}{\sqrt{2}} \left[W_\mu^1 \mp i W_\mu^2 \right] \\ A_\mu &= \cos\theta_W \, B_\mu + \sin\theta_W \, W_\mu^3 \\ Z_\mu &= -\sin\theta_W \, B_\mu + \cos\theta_W \, W_\mu^3 \end{aligned} \tag{2.5}$$

The $W^\pm$ can be interpreted as raising and lowering operators on I_3 mediating transitions within the lefthanded doublets of one fermion generation while A_μ represents the massless photon field and Z_μ a massive neutral boson. The parameter θ_W determines the strength of the mixing and is called electroweak mixing angle or Weinberg angle.

As a result of the mixing between the singlet vector field B and the triplet vector field $\boldsymbol{W}$ the couplings of the gauge bosons to fermions differ. The vertex factors for the different interactions are[2]

$$\begin{aligned} \gamma: &\quad -ieQ_f \gamma^\mu \\ W^\pm: &\quad -i\frac{g}{2}\gamma^\mu \frac{1}{2}(1-\gamma^5) \\ Z: &\quad -i\frac{g}{\cos\theta_W}\gamma^\mu \frac{1}{2}(g_V^f - g_A^f \gamma^5) \end{aligned} \tag{2.6}$$

where $g \sin\theta_W = e$ and the vector and axial-vector couplings, g_V^f and g_A^f are given by:

$$\begin{aligned} g_V^f &= I_3^f - 2\sin^2\theta_W \, Q_f \\ g_A^f &= I_3^f \end{aligned} \tag{2.7}$$

From eq. 2.6 one can see that the photon γ couples only to the electric charge regardless of the handedness of the fermion. The weak charged current has a vector - axial-vector form $(1-\gamma^5)$ and in consequence the $W^\pm$ only couple to left-handed fermions, maximally violating parity conservation. The Z couples to the electric charge Q and the third component of the weak isospin I_3. As I_3 is zero for right-handed fermions the Z couples differently to left- and right-handed fermions. A consequence of this behaviour is that the Z does not couple to right-handed neutrinos. The formalism of electroweak unification described above was first introduced by Salam and Weinberg [6, 7], based on earlier work of Glashow [5].

[2] The γ^μ are the Dirac matrices with $\gamma^5 \equiv i\,\gamma^0\gamma^1\gamma^2\gamma^3$.

2.1.2 The Process $e^+e^- \to \mu^+\mu^-$

In this analysis muon pair production via a virtual γ or Z shall be investigated. This process is described within the framework of the SM by the amplitudes $\mathcal{M}_\gamma$ and $\mathcal{M}_Z$ for the two corresponding Feynman diagrams (see figure 2.1 a))

$$\begin{aligned} \mathcal{M}_\gamma = & \quad -\tfrac{e^2}{k^2}(\bar{\mu}\gamma^\nu\mu)(\bar{e}\gamma_\nu e) \\ \mathcal{M}_Z = & \quad -\tfrac{g^2}{4\cos^2\theta_W}\left[\bar{\mu}\gamma^\nu(g_V^\mu - g_A^\mu\gamma^5)\mu\right]\left(\tfrac{g_{\nu\sigma}-k_\nu k_\sigma/M_Z^2}{k^2-M_Z^2}\right)\left[\bar{e}\gamma_\sigma(g_V^e - g_A^e\gamma^5)e\right] \quad . \end{aligned} \tag{2.8}$$

In the above formulae k is the four-momentum of the virtual γ or Z and hence $k^2 \simeq s = E_{CM}^2$. Furthermore, particle names are used to denote Dirac spinors. Using the Feynman rules and neglecting the fermion masses the Born differential cross section for $e^+e^- \to \mu^+\mu^-$ with unpolarized beams can be calculated as

$$\begin{aligned} \frac{d\sigma^0(s)}{d\cos\theta^*} &= \frac{\pi\alpha^2}{2s}(1+\cos^2\theta^*) \\ &+ \frac{\pi\alpha^2}{2s}Re(Z(s))\left[(1+\cos^2\theta^*)2g_V^e g_V^\mu + 4g_A^e g_A^\mu\cos\theta^*\right] \\ &+ \frac{\pi\alpha^2}{2s}|Z(s)|^2\left[(1+\cos^2\theta^*)(g_V^{e\,2}+g_A^{e\,2})(g_V^{\mu\,2}+g_A^{\mu\,2}) + 8g_V^e g_V^\mu g_A^e g_A^\mu\cos\theta^*\right] \end{aligned} \tag{2.9}$$

where θ^* is the polar angle in the centre-of-mass frame between the incoming electron (e^-) and the outgoing muon (μ^-). The Z propagator in the lowest order Breit-Wigner approximation is given as

$$Z(s) = \frac{s}{s - M_Z^2 + iM_Z\Gamma_Z} \quad . \tag{2.10}$$

Hence the total cross section for this process in the Born approximation is given by

$$\begin{aligned} \sigma_{tot}^0(s) = \quad & \tfrac{4\pi\alpha^2}{2s}\left[1 + (g_V^{e\,2}+g_A^{e\,2})(g_V^{\mu\,2}+g_A^{\mu\,2})\tfrac{s^2}{(s-M_Z^2)^2+M_Z^2\Gamma_Z^2}\right. \\ & \left. +2g_V^e g_V^\mu\tfrac{(s-M_Z^2)^2}{(s-M_Z^2)^2+M_Z^2\Gamma_Z^2}\right] \quad . \end{aligned} \tag{2.11}$$

As the coupling of the Z is a mixture of vector- and axial-vector couplings, parity is not conserved and consequently the angular distribution of the outgoing muons is not symmetric. This manifests itself in the terms proportional to $\cos\theta^*$ in eq. 2.9. By defining the forward-backward asymmetry A_{FB}^0 at Born level as

$$\mathrm{A}_{FB}^0 = \frac{\sigma_F - \sigma_B}{\sigma_F + \sigma_B} \tag{2.12}$$

where σ_F and σ_B are the cross sections in the forward and backward hemispheres respectively, eq. 2.9 can be rewritten as

$$\frac{d\sigma^0(s)}{d\cos\theta^*} = \frac{3}{8}\sigma_{tot}^0(s)\,(1+\cos^2\theta^* + \frac{8}{3}A_{FB}^0(s)\cos\theta^*) \quad . \tag{2.13}$$

The asymmetry varies strongly with s and it arises far above or below the Z-peak from the interference of the electromagnetic vector- and the weak axial-vector-interaction while at the Z-peak the asymmetry stems from interference between the weak vector- and axial-vector-interaction.

2.1.3 Radiative Corrections

All the results obtained so far were derived in the lowest order of the electroweak theory neglecting radiative corrections. However, contributions from diagrams of higher order play an important role as they change the size of the investigated physical quantities. The higher order corrections can be divided into two separate classes - purely electromagnetic and electroweak corrections.

The purely electromagnetic corrections include diagrams with either real photons or virtual photons. The radiation of external photons can either occur in the initial state (ISR) or in the final state (FSR). Most ISR photons are emitted in the direction of the incoming electron or positron and therefore vanish in the beam pipe. This is not necessarily the case for FSR photons, which usually can be seen in the detector. Virtual photons start and terminate at external fermions and include box diagrams with the exchange of either two virtual photons or one virtual photon and one massive boson.

For the electroweak radiative corrections only diagrams where virtual weak vector bosons are exchanged have to be considered at the centre-of-mass energies investigated in this analysis. The electroweak corrections include loop corrections, which modify the vector boson propagators or the vertex diagrams. A further contribution comes from box diagrams where two massive vector bosons are exchanged.

In order to account for most of the higher order effects, the program ZFITTER (v.6.23) [15] is used to calculate the SM cross sections and asymmetries. It includes all the $\mathcal{O}(\alpha)$ QED and electroweak loop corrections, e.g. ISR, FSR and the interference between these two processes. Furthermore, those higher order terms that provide the largest contributions are included as well. A theoretical treatment of radiative corrections can be found in [16].

2.2 Definitions of Cross Sections and Asymmetry

The measurement of cross sections and asymmetries presents a good possibility to test the structure of the SM. In order to measure the dimuon cross section, those events are considered where electron and positron annihilate into a virtual γ or Z, which subsequently decay into a muon-pair. This means that also events with multiple ISR or FSR are taken into account.

Two cross sections are defined for two different regions of phase space. An inclusive cross section is determined, including events with hard ISR. This measurement allows to test the theoretical predictions for radiative corrections according to QED. For the exclusive cross section events with high invariant mass M_{inv} of the muon pair are selected in order to look for new physical phenomena that would arise at high energy scales. Feynman diagrams for the considered processes, one at centre-of-mass energy and one with ISR, are shown in figure 2.1.

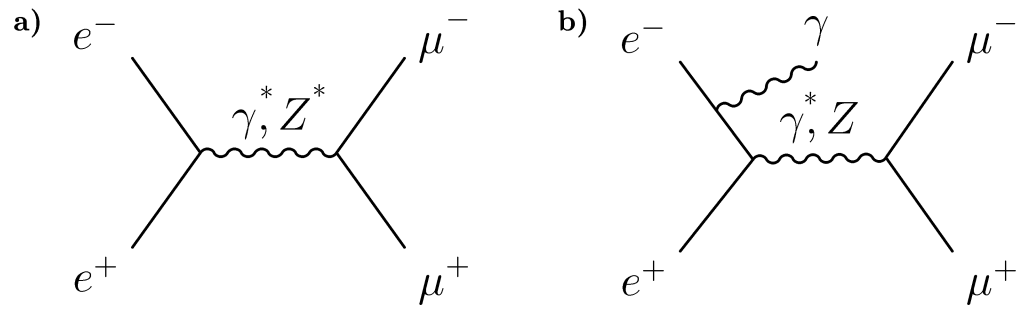

Figure 2.1:
Dimuon production at LEP 2. Figure a) shows an event at centre-of-mass energy. In figure b) an event with ISR is displayed. Depending on the energy of the ISR photon the Z can be either virtual or real.

Inclusive Cross Section

The inclusive cross section is defined for the region $\sqrt{s'/s} > 0.1$ and the full solid angle. The variable s' is the square of the invariant mass M_{inv} of the outgoing muon pair and $s = E_{CM}^2$. It includes events with hard ISR and a large part of the considered events are so called 'radiative returns to the Z', where in the initial state one or more hard photons are emitted, so that the invariant mass of the remaining system is boosted back to the Z-resonance.

Exclusive Cross Section

The exclusive cross is defined for the region $\sqrt{s'/s} > 0.9$ and only for a polar region of $|\cos\theta| < 0.95$, θ being the polar angle in the detector frame. The reason for this restriction is that ISR/FSR interference effects, which are especially prominent in the forward direction, are theoretically not yet precisely calculated in this region.

For the event selection the variable s'_m is used which is equal to s' when (multiple) ISR from either the electron **or** the positron is present. s'_m is determined through an angle measurement which is much more precise than the momentum measurement. Explicitly,

$$s'_m = \frac{\sin\theta_1 + \sin\theta_2 - |\sin(\theta_1 + \theta_2)|}{\sin\theta_1 + \sin\theta_2 + |\sin(\theta_1 + \theta_2)|} \cdot s \tag{2.14}$$

where θ_1 and θ_2 are the polar angles of the two muons. These polar angles have to be measured with respect to the direction of a possibly emitted photon as illustrated in figure 2.2. If the ISR photon is seen in the detector, its reconstructed direction is taken as reference. Otherwise the photon is assumed to be emitted along the beam-pipe and so the angles are measured with respect to the e^- direction.

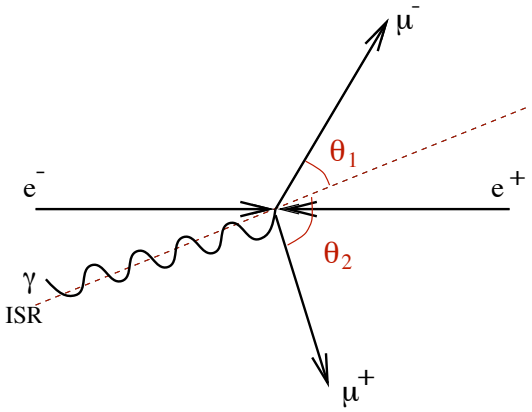

Figure 2.2:
Definition of the angles used for the calculation of s'_m in the case of a reconstructed ISR photon.

In the case of ISR from both the electron and the positron the variable s'_m is not equal to s anymore. Events with such a topology are called 'double radiative events'. If both photons have roughly the same energy, the centre-of-mass frame is still equal to the laboratory frame although E_{CM} is lower than twice the nominal LEP energy, i.e. $s' < s$. Hence, the event will not be boosted but the two final state muons will be back-to-back and therefore have a high $\sqrt{s'_m/s}$ because this is a measurement of the acollinearity. A schematic illustration is given in figure 2.3.

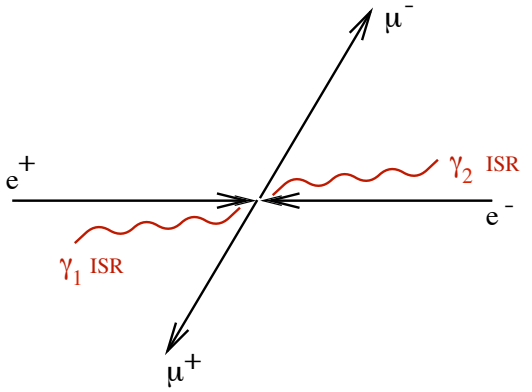

Figure 2.3:
Topology of a double radiative event. Electron and positron emit photons of roughly the same energy in the initial state so that the outgoing fermion pair is still back-to-back.

Asymmetry

The asymmetry A_{FB} is a function of the centre-of-mass energy $\sqrt{s}$. In this analysis it is only determined for the exclusive sample which means that it is measured at high centre-of-mass energies. As mentioned before, one effect of ISR is that events get boosted and therefore the detector frame and the centre-of-mass frame are not the same anymore. For this reason the angle of the outgoing μ^- with respect to the e^- direction has to be measured in the $\mu^+\mu^-$ rest frame. This polar angle is called θ^* and can be obtained from the angles θ_+ and θ_-, which

are the polar angles of the positively and negatively charged muon respectively, according to the formula

$$\cos\theta^* = \frac{\sin\frac{1}{2}(\theta_+ - \theta_-)}{\sin\frac{1}{2}(\theta_+ + \theta_-)} \quad . \tag{2.15}$$

In order to demonstrate the accuracy of the angle measurement, the difference between the generated and reconstructed θ^* is shown in figure 2.4 (based on MC simulations). The resolution in θ^* is approximately 0.07 *mrad*.

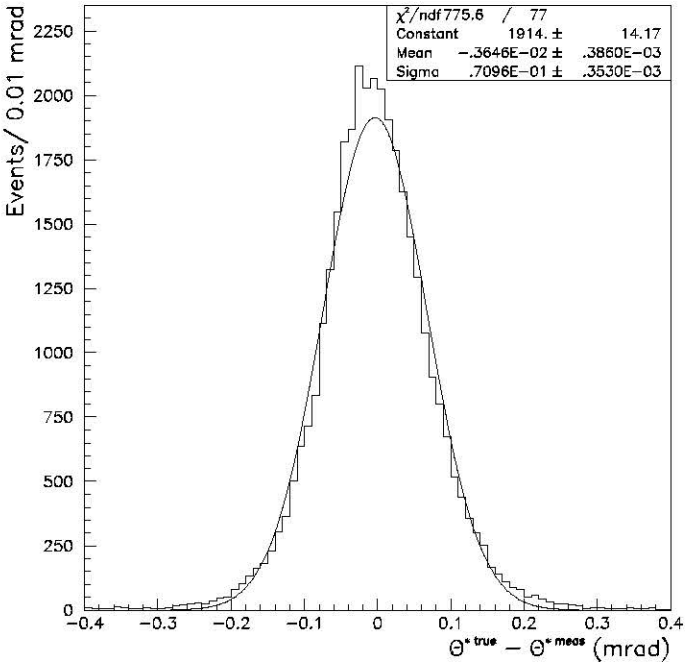

Figure 2.4:
Resolution of θ^* in mrad. The diagram shows the difference between the generated and reconstructed θ^*. A gaussian distribution was fitted to the MC distribution with a resulting width of 0.07 mrad.

2.3 Physics Beyond the Standard Model

Although the predictions of the SM agree with experiments up to fantastic precision [17, 18], it is not considered to be the 'final' theory. The SM cannot provide solutions to crucial problems like the electroweak symmetry breaking or the hierarchy problem. As already mentioned, measurements of cross sections and angular distributions present good possibilities to test the SM predictions. With the appearance of new particles or interactions the cross sections and angular distributions predicted by the SM would be altered.

For this reason extra terms describing phenomena beyond the physics of the SM are added to

the SM Lagrangian. From deviations between the measured cross sections and asymmetries and the SM predictions limits on the energy scale can be derived where these new phenomena or their respective couplings would arise. In chapter 6 a short description of the theoretical ideas behind two specific models, namely Contact Interactions and TeV-Scale Quantum Gravity, is given and limits on the energy scale where these phenomena could appear are derived.

Chapter 3

The ALEPH Experiment at LEP

In this chapter a short survey of the experimental environment is given. This includes the LEP collider and the detector ALEPH.

3.1 LEP Collider

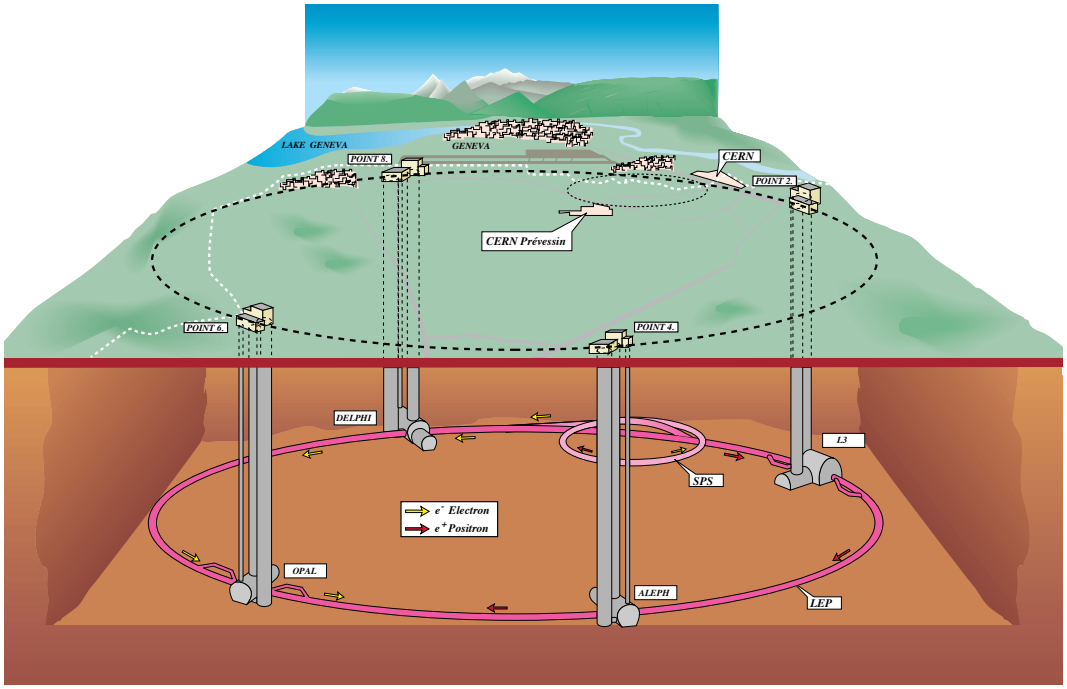

Figure 3.1: *The LEP Collider.*

The LEP collider is installed in a tunnel of 26.7 km circumference, 80 - 150 m underground (see figure 3.1). The large size is necessary to limit the energy loss due to sychrotron radiation of electrons and positrons which is proportional to $\frac{E^4}{m^4\rho}$, E being the energy of the particle, m the mass and ρ the bending radius. Four bunches of each type with about 10^{12} particles are injected into LEP in opposite directions with an energy of 22 GeV and are then accelerated to the final energy. The bunches are brought into collision every 22 μs at four interaction points

inside the detectors of the LEP experiments ALEPH, DELPHI, L3 and OPAL. LEP was built in order to investigate the properties of the weak vectorbosons and ran from 1989 -1995 at the Z-resonance allowing a precise measurement of many observables, e.g. the Z mass and width. Meanwhile LEP is running at centre-of-mass energies above 205 GeV and is therefore permitting additional studies of W and Z pair production and triple gauge couplings. A detailed description of the LEP collider is given in [19].

3.2 ALEPH Detector

The ALEPH detector is designed to study all types of SM processes at LEP and to search for new phenomena. For this purpose it covers as much as possible of the 4π solid angle and consists of several subdetectors. Tracking detectors permit measurements of the momenta of charged particles and with calorimeters the energy of charged and neutral particles can be evaluated. A cut-away view of ALEPH displaying the subdetectors is given in figure 3.2. The structure of ALEPH is cylindrical around the beam axis therefore suggesting a cylindrical coordinate system with the beam-axis as z-direction and the interaction point as origin. For analysis purposes the positive z-direction is taken along the incoming e^--beam and the polar angle θ of the momentum vector at the origin of the tracks is measured with respect to this axis. The distance of closest approach to the beam-axis is denoted by d_0 while z_0 gives the z-coordinate of the respective point.

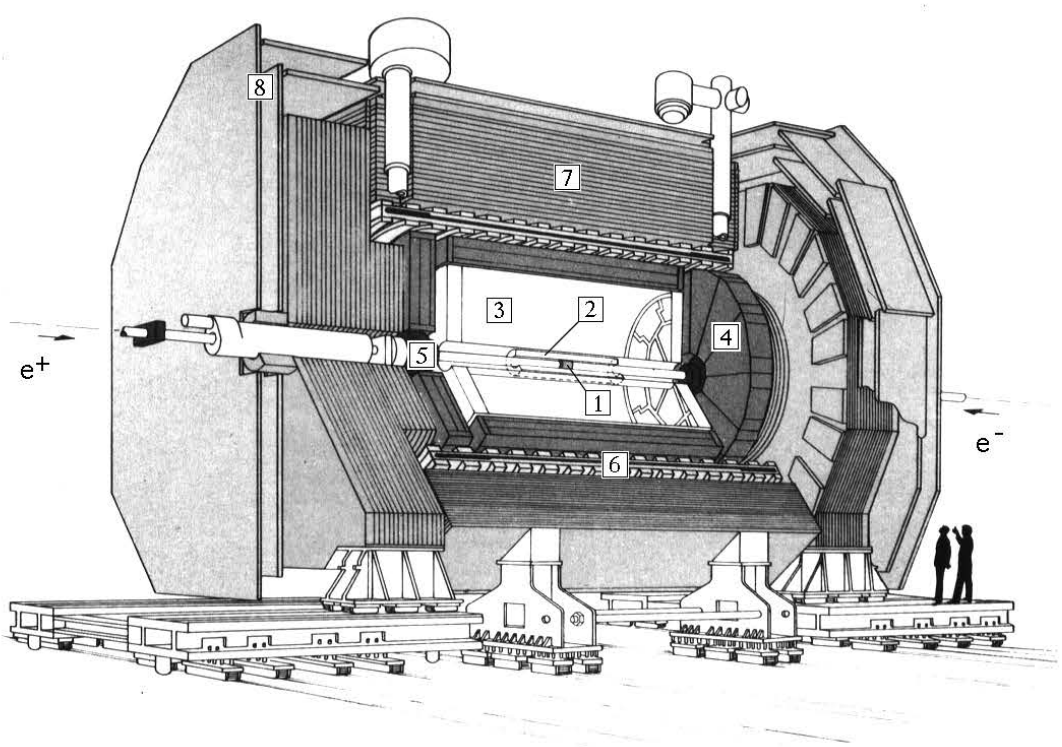

Figure 3.2:
The ALEPH-Detector. [1]*: Vertexdetector, VDET.* [2]*: Inner Tracking Chamber, ITC.* [3]*: Time Projection Chamber, TPC.* [4]*: Electromagnetic Calorimeter, ECAL.* [5]*: Luminositycalorimeter, LCAL.* [6]*: Magnet Coil.* [7]*: Hadron Calorimeter, HCAL.* [8]*: Muon Chambers, MUON.*

Close to the beam-axis are three tracking detectors, a vertex detector (VDET), the inner tracking chamber (ITC) and the time projection chamber (TPC). The TPC is surrounded by the electromagnetic calorimeter (ECAL). All these detector components are immersed by a homogeneous magnetic field of 1.5 $Tesla$ parallel to the z-axis, which is generated by a superconducting magnet coil. Outside the magnet coil the hadron calorimeter (HCAL) follows, which is surrounded by the muon chambers (MUON). The different components shall be briefly discussed in the following. A detailed description of the detector and its performance is given in [20] and [21] respectively.

3.2.1 Tracking Detectors

Vertex Detector (VDET)

The vertex detector is composed out of two concentric layers of silicon wafers at 6.3 and 10.8 cm around the beam-pipe. The wafers have perpendicular readout strips on both sides and therefore the position of a particle can be determined simultaneously in two directions. The angular acceptance is $|\cos\theta| \leq 0.95$ if a particle is only required to pass through the inner VDET layer. In order to reconstruct secondary vertices properly, a very good spatial resolution is required. For perpendicular penetrating muons the resolution in the $r\phi$-direction is $\sigma_{r\phi} \approx 12\mu m$ and in the z-direction $\sigma_z \approx 10\mu m$.

Inner Tracking Chamber (ITC)

The ITC is a conventional multiwire drift chamber of 2 m length and an outer radius of 28.8 cm. It has 960 sense wires arranged in 8 concentric cylindrical layers. Each sense wire is surrounded by 6 earthed wires to form a hexagonal drift cell. The ITC is filled with an $Ar - CO_2$ gas mixture. The main purpuse is to measure the $r\phi$ position of a charged particle track with high precision. From the drift time of the ionized electrons and the position of the sense wires a $r\phi$ coordinate can be measured with an average precision of 150 μm. The z-coordinate can be measured from the difference between the arrival times of the electrical pulses at the two ends of the wires but is not very precise ($\sigma_z = 7$ cm). The ITC can cover a polar angle of $|\cos\theta| \leq 0.97$ with all eight layers being traversed by a charged particle.

Time Projection Chamber (TPC)

The TPC, shown in figure 3.3, allows to measure many space points along a charged particle's track. The chamber is 4.7 m long and has inner and outer radii of 31 cm and 1.8 m respectively. The electric drift field extends from each end plate towards a central membrane that intersects the chamber and is held at -47 kV. The TPC is filled with an $Ar - CH_4$ gas mixture that gets ionized when charged particles traverse the chamber. Electrons from ionization drift along the electric field towards the end-plates, which are equipped with multiwire proportional chambers. Cathode pads underneath the sense wires collect an induced signal and an accurate measurement of the $r\phi$ coordinate of the track is achieved by interpolating between the signal on different pads. The z-coordinate can be extracted from the arrival time due to the constant drift velocity of 5.2 $cm/\mu s$. Since the magnetic field is along the beam-axis just like the electric field, the electrons drift in tight spirals towards the end-plates and the $r\phi$ information is maintained. A maximum of 21 space points (according to 21 concentric rings of pads) can be measured with a resolution of $\sigma_{r\phi} \approx 173$ μm and $\sigma_z \approx 740$ μm. Additionally, the TPC provides dE/dx (energy loss) information, which can be used to determine the

particle velocity, and together with its momentum indicates the particle type.

Combining all the three tracking detectors a transverse momentum resolution of

$$\frac{\sigma_{p_T}}{p_T} = 0.6 \times 10^{-3} \times p_T \ (GeV/c)^{-1}$$

is achieved (determined from muons with $p_T \approx 45\ GeV/c$, p_T being the momentum transverse to the beam-axis).

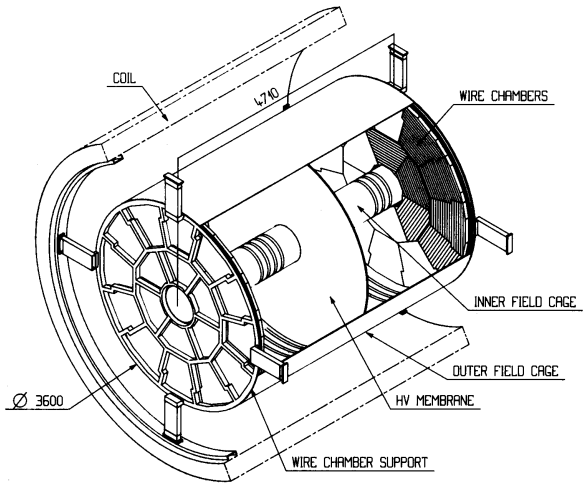

Figure 3.3:
Structure of the Time Projection Chamber with the wire chambers of each end indicated. The inner and outer field cage are also shown as well as the central membrane.

3.2.2 Calorimeters

Electromagnetic Calorimeter (ECAL)

The ECAL consists of a central barrel, still inside the superconducting magnet coil, and end-caps at both sides of the detector. All the three parts consist of 12 modules covering an azimuthal angle of 30°. Each module is a 45 layer lead/proportional chamber sandwich. The energy and the direction of the incident particle can be determined for charged and neutral particles. Furthermore, the shape of the electromagnetic shower can be used for particle identification. The energy resolution in the barrel and the central region of the end-caps of ECAL is

$$\frac{\sigma_E}{E} = 0.009 + \frac{0.18}{\sqrt{E/GeV}}$$

The angular resolution of the calorimeter is

$$\sigma_\phi = \frac{\sigma_\theta}{\sin\theta} = (0.25 + \frac{2.5}{\sqrt{E/GeV}})mrad$$

Hadron Calorimeter (HCAL) and Muon Chambers (MUON)

The structure of HCAL, shown in figure 3.4, is similar to ECAL apart from the end-caps that are only subdivided into six modules. Barrel and end-caps consist of 23 layers of iron of 5 *cm* thickness and gas-filled streamer tubes. As HCAL is outside the magnet coil the iron layers provide a return path for the magnetic flux lines. The iron is used as shower material and with the streamer tubes the energy deposit of hadronic objects can be determined. The basic element is a wire counter made of a graphite-coated plastic tube operated in limited streamer mode. The energy of charged and neutral particles can be measured in HCAL with a resolution of

$$\frac{\sigma_E}{E} = \frac{0.85}{\sqrt{E/GeV}}$$

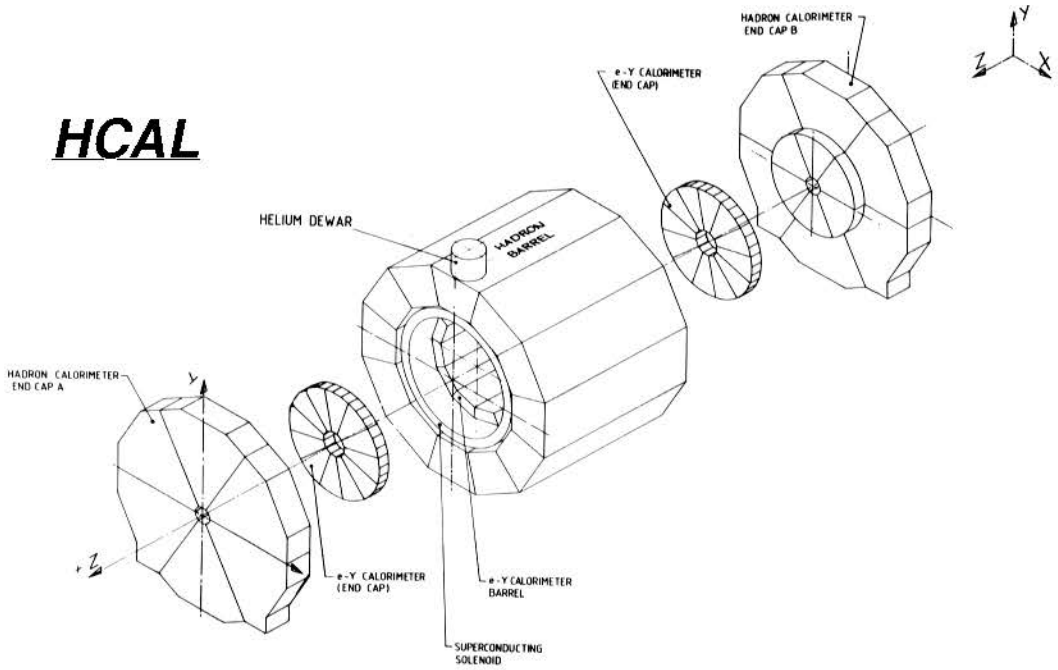

Figure 3.4: *The Hadron Calorimeter with barrel and end-caps.*

Outside HCAL two layers of muon chambers (MUON) are attached. They consist of two planes of double-layer streamer tubes which are separated by 40−50 *cm*. The chambers do not provide an energy measurement but give spatial information as the wires of the double-layers are orthogonal. Signals in MUON that are associated to a track recorded in the tracking detectors can only come from muons as all other particles get absorbed in the calorimeters.

Luminosity Detectors (LCAL, BCAL, SICAL)

For precise cross section measurements, an accurate knowledge of the luminosity is essential and for this reason ALEPH is equipped with several luminosity calorimeters.
The Luminosity CALorimeter (LCAL) is a sampling calorimeter placed around the beam pipe at both ends of the detector consisting of lead sheets and wire chambers of 38 layers. It covers the polar angle region from 45 to 160 *mrad*. It is used in this analysis to calculate

the luminosity, which is basically done by counting the number of Bhabha events for which there are two back-to-back deposits of energy compatible with the beam energy.
The Bhabha CALorimeter (BCAL) and the Silicon CALorimeter (SiCAL) are used for the online luminosity measurement. BCAL is located further away from the detector, therefore covering smaller angles. The latter applies to SiCAL as well which is closer to the interaction point than LCAL but closer to the beam-pipe. They are partly used as background monitors and as a systematic check for the LCAL measurement.

Chapter 4

Event Selection

The identification of a dimuon event in the detector is rather simple as its signature is very clean. Muons are deeply-penetrating, minimum ionizing particles and so one looks for two tracks of opposite charge that give signals in the outer planes of HCAL or in MUON (see figure 4.1). The details of the selection are outlined in this chapter.

4.1 Muon Identification

The event selection follows a procedure described in [22] and [23]. The identification of single muons and afterwards muon pairs requires a set of steps. Since muons are charged particles, they will ionize the gas in the ITC and TPC and therefore produce a set of space points which can be combined to form a track. These tracks should originate from a region close to the interaction point whereas beam gas and cosmic events cause tracks whose origin is not necessarily the interaction point. In consequence, the first task is to identify so called "good" tracks in an event. This is done by requiring the following criteria to be fulfilled:

- the distance d_0 of closest approach to the beam axis has to be shorter than 2.0 cm,
- the distance to the nominal interaction point in z-direction z_0 has to be shorter than 10.0 cm,
- $|\cos\theta| \leq 0.95$ where θ is the polar angle in the laboratory frame,
- more than four hits (space points) in the TPC.

In a further preselection the conditions are tightened by requiring each track to have at least a momentum of 6 GeV/c and four associated hits in the ITC.

Compared to electrons the Bremsstrahlung process for muons is suppressed when interacting with matter due to their higher mass. In consequence, they are much more penetrating and therefore one looks for associated signals in the outer layers of HCAL and in MUON. In order to be identified as a muon, a track has to pass one of three independent selections. Two are based on digital hit patterns in HCAL and MUON respectively while the third is a calorimetric selection based on the energy deposit in ECAL and HCAL. In detail the following requirements have to be satisfied:

1. One or more space points in MUON associated to the track

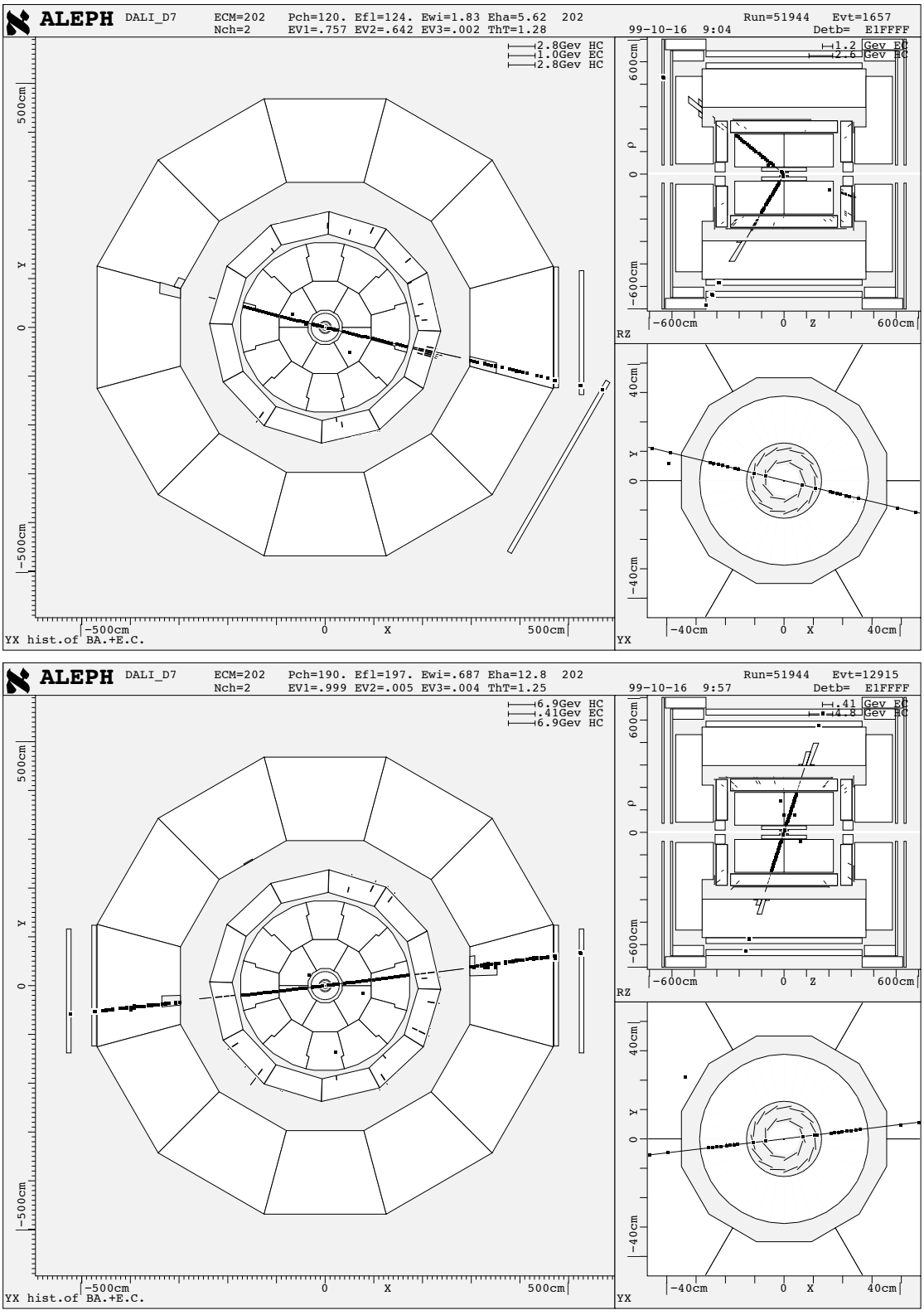

Made on 17-Jun-2000 17:00:57 by flaecher with DALI_D7.
Filename: DG051944_001657_**0617_1700.PS

Made on 17-Jun-2000 17:08:04 by flaecher with DALI_D7.
Filename: DG051944_012915_**0617_1708.PS

Figure 4.1: *ALEPH display of two* $e^+e^- \to \mu^+\mu^-$ *candidates. The upper picture shows an event from the inclusive selection where the boost of the event is apparent while the lower picture shows an exclusive event. The big window and the one on the lower right give r-*ϕ*-views while in the top right corner a r-z-view of the detector is shown. The hits in the TPC, HCAL and MUON (left) and the ITC (lower right) are clearly visible.*

2. Signals in HCAL (depth information):
   - 10 out of 23 streamer tube planes and
   - 50 % of the planes the track is expected to cross and
   - 3 or more of the outermost 10 planes
3. Energy deposit in ECAL and HCAL (minimum ionizing particle):
   - ECAL + HCAL energy is less than 60 % of the track's momentum and
   - ECAL energies + track momenta are less than 60 % of the LEP energy E_{CM} and
   - at least one hit in the outermost 10 planes of HCAL that is associated to the track

4.2 Dimuon Selection

From the remaining events only those that contain at least two muon candidates are kept. A standard selection procedure to identify dilepton candidates is applied. Events passing this selection are flagged as 'class15'. The precise cuts for this event class are described in [24]. In the next step the two most energetic muons of opposite charge are selected. To discriminate against cosmic muons even stricter cuts are imposed on the primary vertex, namely $|d_0(\mu_1)| + |d_0(\mu_2)| < 1.0$ cm and $|z_0(\mu_1)| + |z_0(\mu_2)| < 5.0$ cm.

As the cross section is measured for two regions of phase space, which was already explained in chapter 2.2, the event selection follows different procedures at this stage.

The cuts on invariant mass and sum of the energies of the two muons are the following:

- inclusive sample:
  The sum of the energies of the two muons as well as the invariant mass of the outgoing muon pair have to exceed 60 $GeV(/c^2)$ each. This is done to reduce background from $\gamma\gamma \to \mu^+\mu^-$.
- exclusive sample:
  The sum of the energies of the two muons as well as the invariant mass of the outgoing muon pair have to exceed 150 $GeV(/c^2)$ each. In addition $\sqrt{s'/s}$ has to be larger than 0.9. These cuts remove events with hard ISR.

4.3 Acceptance and Efficiency

For the two ranges in $\sqrt{s'/s}$ different acceptances are defined. The inclusive sample contains all events with $\sqrt{s'/s} > 0.1$ while the exclusive sample includes events with $|cos\theta| < 0.95$ and $\sqrt{s'/s} > 0.9$.

In order to determine the efficiency of the selection, MC simulations are used. As the detector has only a finite resolution, cracks and insensitive regions, one never fully reconstructs all events. In addition, the reconstruction of observables is never exact either. All these effects are simulated and one compares the number of generated events with the number of events which pass the full reconstruction and selection. The efficiency of the selection is defined as the ratio between selected events and the total number of events generated in the respective

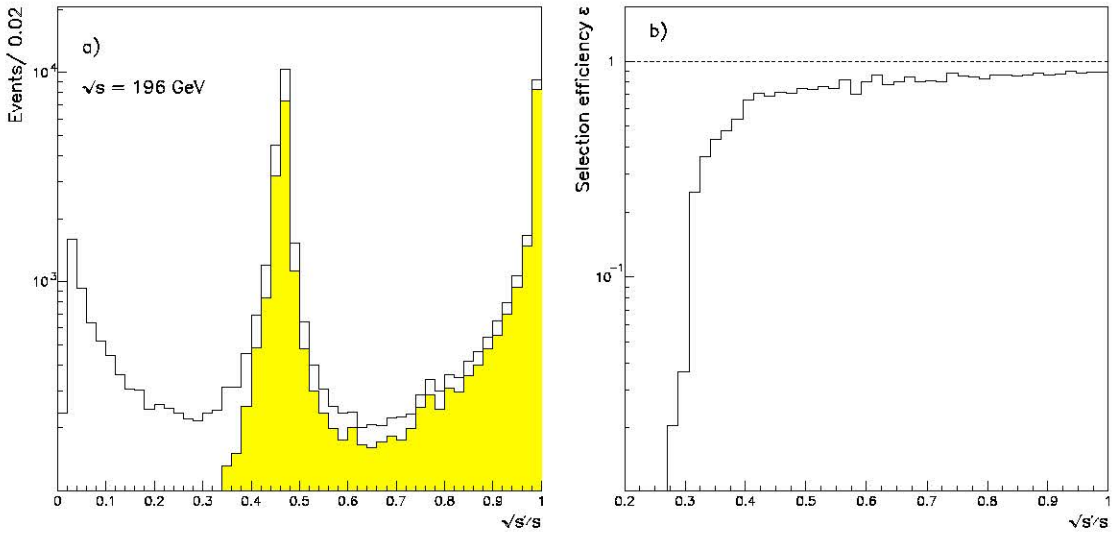

Figure 4.2:
Figure a) the white histogram shows the true $\sqrt{s'/s}$ distribution for the generated events while the grey histogram shows the fraction of the selected events for the inclusive selection. In figure b) the selection efficiency as a function of $\sqrt{s'/s}$ is displayed. One can see that the selection efficiency decreases at a value of $\sqrt{s'/s} \approx 0.4$ and drops to zero just below 0.3.

region defined by the acceptance criteria. In figure 4.2 the efficiency as a function of $\sqrt{s'/s}$ is shown and along with it the true $\sqrt{s'/s}$ distribution for all generated and selected events. One can see that the efficiency decreases at a value of $\sqrt{s'/s} \approx 0.4$ and goes down to zero just below 0.3. The reason for this is that a cut in the measured invariant mass at 60 GeV/c^2 (which corresponds to $\sqrt{s'/s} \approx 0.3$) is made in order to discriminate against background from $e^+e^- \to \gamma\gamma$. In order to elucidate the drastic decrease of the selection efficiency, the resolution of the invariant mass M_{inv} is shown in figure 4.3. It is of the order of $2-3$ % and this explains the rapid decrease of the efficiency. As expected, the resolution gets worse with higher invariant mass and thus higher momenta of the muons. Histogram a) of figure 4.3 shows the resolution of the invariant mass for Z-return events in a window between 85 and 97 GeV/c^2 while in histogram b) the resolution for events with $M_{inv} > 185$ GeV/c^2 is displayed. Diagram c) shows the variation of the resolution as a function of M_{inv}.

In table 4.1 the efficiencies for the inclusive and exclusive selections are given. The differences arise because of the different definitions of the acceptance.

E_{CM}	Selection efficiency (%) $\sqrt{s'/s} > 0.1$	Selection efficiency (%) $\sqrt{s'/s} > 0.9$
196 GeV	73.9 ± 0.2	96.1 ± 0.2
200 GeV	73.9 ± 0.3	96.2 ± 0.2
202 GeV	73.2 ± 0.2	96.1 ± 0.2

Table 4.1:
Selection efficiencies for the two $\sqrt{s'/s}$ ranges. The efficiencies for $\sqrt{s'/s} > 0.1$ are calculated for the full solid angle while for $\sqrt{s'/s} > 0.9$ they are restricted to the region $|cos\theta| > 0.95$.

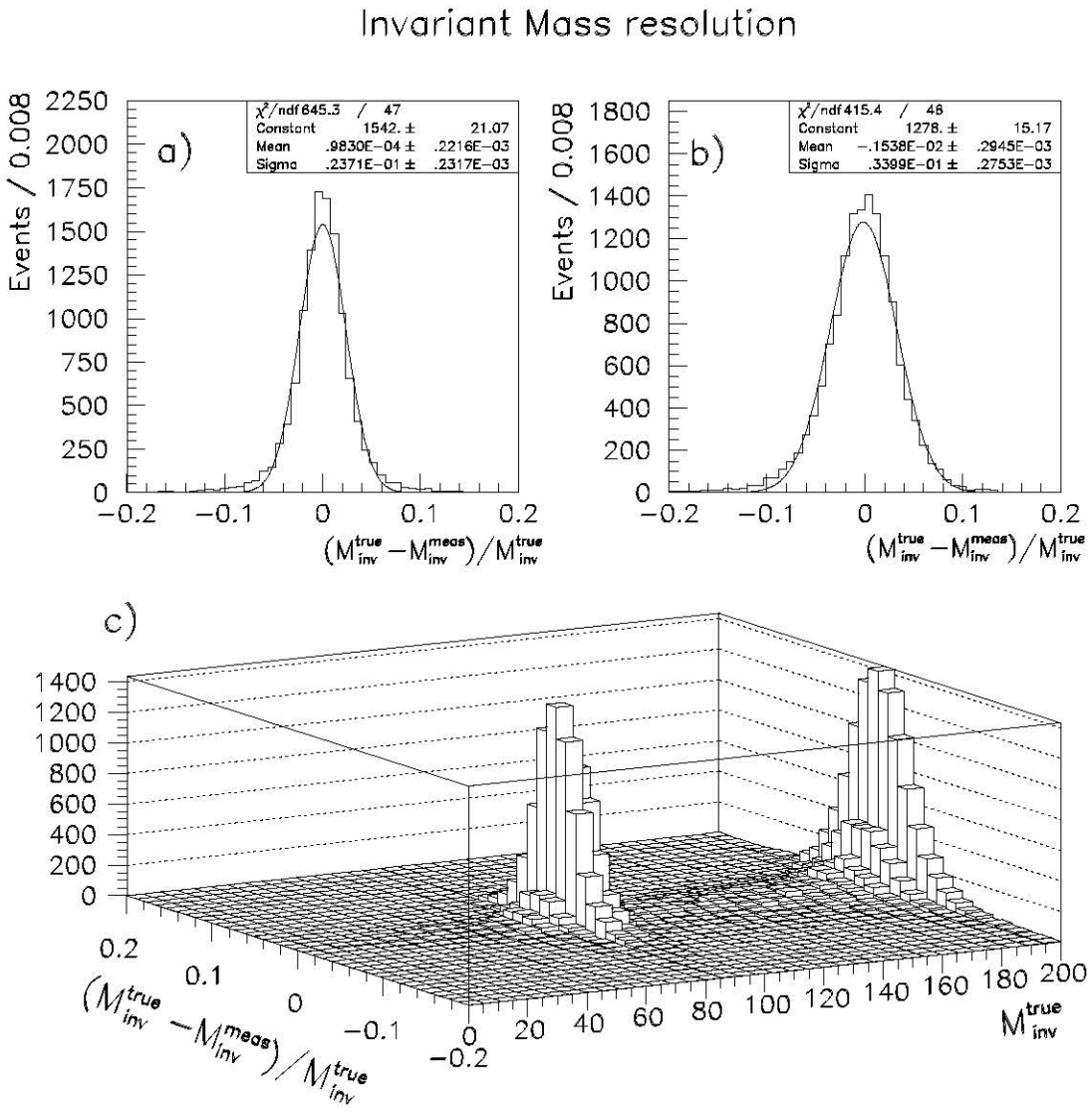

Figure 4.3:
Figure a) shows the resolution of the invariant mass M_{inv} at the Z-peak while in figure b) the resolution for the high-energetic events is shown. To both histograms a gaussian distribution is fitted giving a resolution of $2-3\%$. In figure c) the variation of the resolution for the invariant mass of the muon pair as a function of M_{inv} is shown. It gets worse with higher invariant masses and thus with higher momenta of the muons.

4.4 Background Estimation

Although the previously described selection procedure provides a very good efficiency for muon identification, there are still events originating from other physics processes that pass the applied cuts. The contributions of these processes were estimated with the help of MC simulations. Table 4.2 shows the number of generated MC events and the ratio of the integrated data and MC luminosities for each channel. The background contributions from all the different channels are summarized in table 4.3.

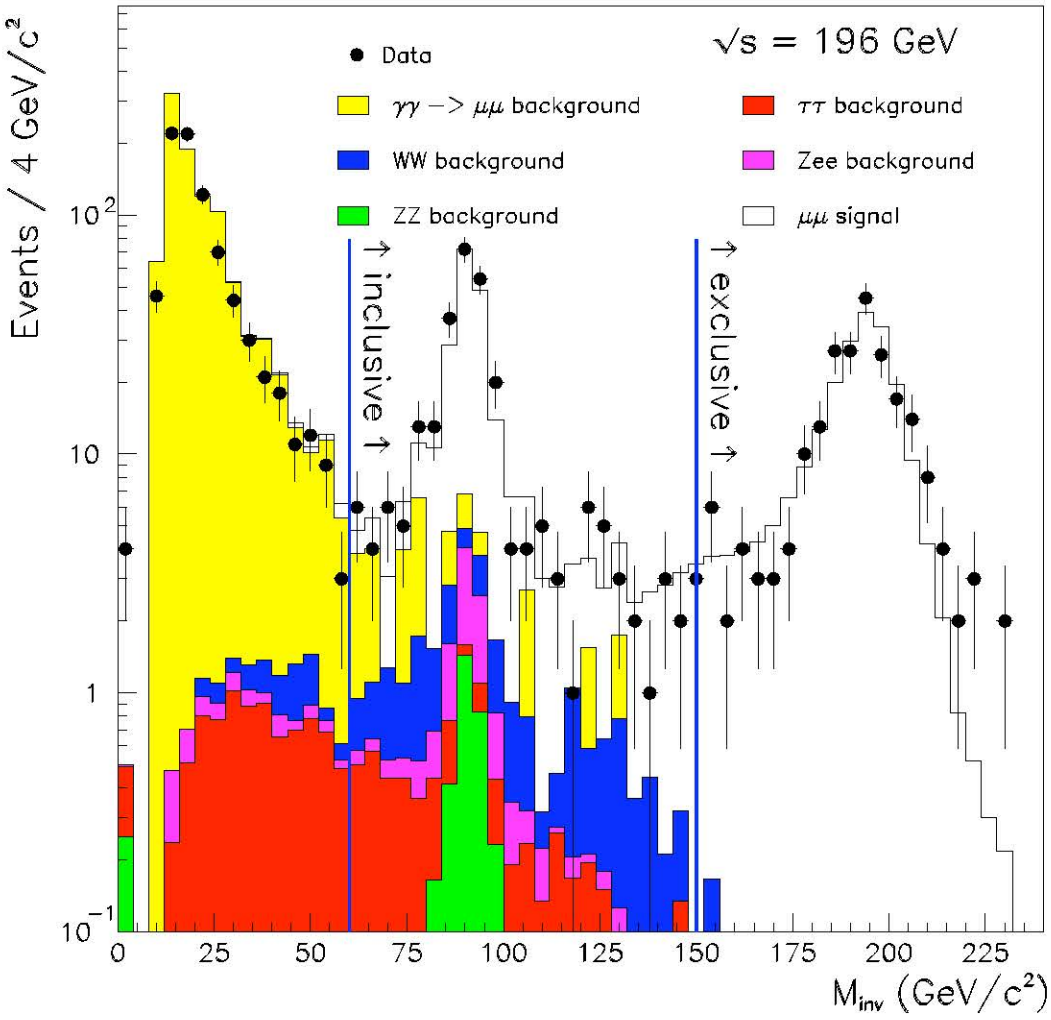

Figure 4.4:
Invariant mass spectrum for E_{CM} = 196 GeV. Shown are data (dots) and MC predictions for signal and background (histograms) with all cuts applied except for the one in the invariant mass of the outgoing muon pair. The two lines indicate the cuts applied for the inclusive and exclusive selection. Here and in the following chapters the different shadings show the accumulated contributions from different channels.

Channel	196 GeV		200 GeV		202 GeV	
	# events	L^{Data}/L^{MC}	# events	L^{Data}/L^{MC}	# events	L^{Data}/L^{MC}
$\mu\mu$	50000	0.012	30000	0.021	50000	0.006
$\gamma\gamma \to \mu\mu$	300000	0.793	300000[1]	0.866	300000	0.421
$\tau\tau$	50000	0.012	30000	0.021	50000	0.006
WW	15000	0.094	20000	0.077	20000	0.038
ZZ	50000	0.005	50000	0.005	50000	0.002
Zee	100000	0.006	100000	0.006	100000	0.003
$Z\nu\nu$	20000	0.000[2]	20000	0.000	20000	0.000
$We\nu$	20000	0.003	20000	0.004	20000	0.002
$q\bar{q}$	100000	0.072	—	—	—	—
$Bhabha$	200000	0.357	200000	0.371	200000	0.177

Table 4.2:
MC events and weight factors (L^{Data}/L^{MC}) for all the investigated background channels. The dash indicates that no background MC was studied. Nevertheless, the 196 GeV MC sample shows that no event passed the selection.

4.4.1 Background from two-photon exchange events

As can be seen from figure 4.4, muon pairs in the final state originating from $e^+e^- \to \gamma\gamma \to e^+e^-\mu^+\mu^-$ constitute one of the main backgrounds in the inclusive sample. In the exclusive sample it is rejected by requiring an invariant mass of 150 GeV/c^2 for the outgoing muon pair. The events were produced with the MC generator PHOT02 [25]. From figure 4.4 one can see that in a region below 60 GeV/c^2 this process is dominant and so it is possible to compare the MC predictions directly with the data. This was done for all the energies in a window from 20 - 60 GeV and is presented in figure 4.5.
As one can see, the MC predictions overestimate the number of events selected in the data. The excess in this window, averaged over all the energies, is about 17.5 %. This is a rather large discrepancy and it was tried to investigate its origin but no satisfactory answer could be found so far. Nonetheless, the shape of the MC prediction is fine, which can be seen from figure 4.5. The background contribution in the selection region was corrected for this excess and the error on it was treated as a systematic uncertainty on this background. This is outlined in more detail in chapter 5.3, where the systematic errors are discussed.

4.4.2 Background from other processes

Apart from $\gamma\gamma \to \mu^+\mu^-$, events from several other processes contribute to the background as well. Bhabha events simulated with the MC generator BHWIDE [26] were investigated but were found to be completely rejected by requiring signals in the last planes of HCAL. Hadronic final states were simulated with the generator PYTHIA [27]. As $q\bar{q}$ final states tend to have high multiplicities and the muon selection requires an invariant mass of at least 60 GeV/c^2 for the two muon candidates, none out of 100000 generated events passed the applied cuts.

[1] $\gamma\gamma \to \mu\mu$ events generated at 202 GeV
[2] L^{Data}/L^{MC} is zero for the quoted precision

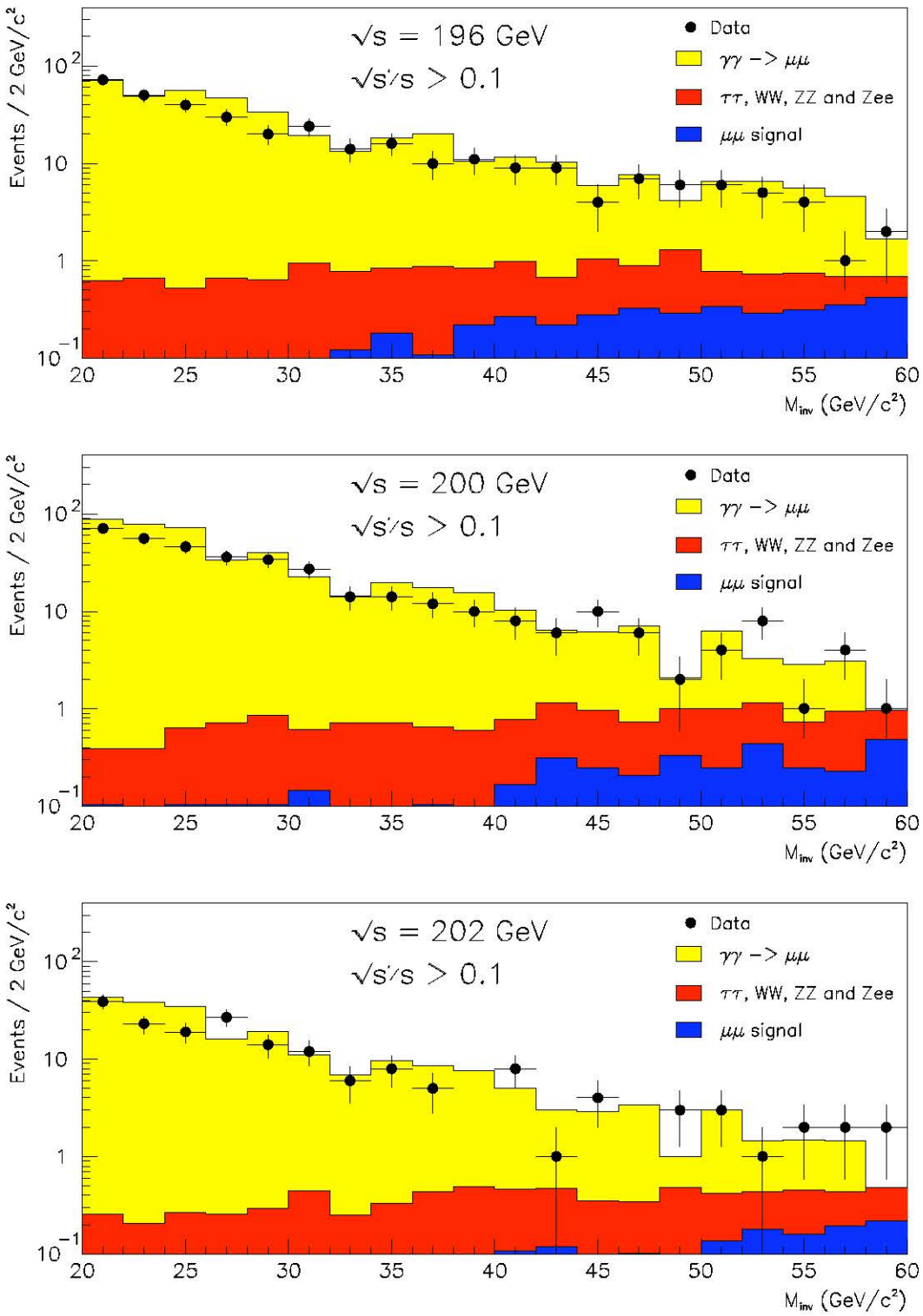

Figure 4.5:
Invariant mass distribution in a region where the $e^+e^- \to e^+e^-\mu^+\mu^-$ process is dominant. Shown are MC predictions for various processes (histograms) and data (dots).

Events from $e^+e^- \to \tau^+\tau^-$ were simulated with KORALZ [28] and they supply a source of background when both tau leptons decay into muons. The branching ratio for a tau to decay into a muon is 17.35 % and so approximately 3 % of the ditau events have two muons in the final state.

The considered centre-of-mass energies are above the WW and ZZ production thresholds. Therefore W-bosons decaying into muons provide an additional source of background as well as one Z decaying into a muon pair while the second decays into neutrinos. The WW background was simulated with KORALW [29]. The PYTHIA generator was used to determine background contributions from the processes $e^+e^- \to ZZ$ and furthermore from $e^+e^- \to Zee$, $Z\nu\nu$ and $We\nu$, the latter two having been found to be negligible. Their contributions to the total background are shown in figure 4.4.

4.4.3 Double Radiative Events

Double radiative events constitute an additional background for the exclusive selection. As one can see from eq. 2.14, $\sqrt{s'/s}$ is obtained from the polar angles of the two muons and not from their momenta. Consequently, the real invariant mass of double radiative events is different from what one calculates. For this reason these events contribute to the background of the exclusive sample now while they are signal events in the inclusive sample. Double radiative events are the main background source in the exclusive sample and their amount is determined with the help of MC simulations because here the true invariant mass is known. The results are summarized in table 4.3 and the true invariant mass distribution of the selected double radiative events is shown in figure 4.6.

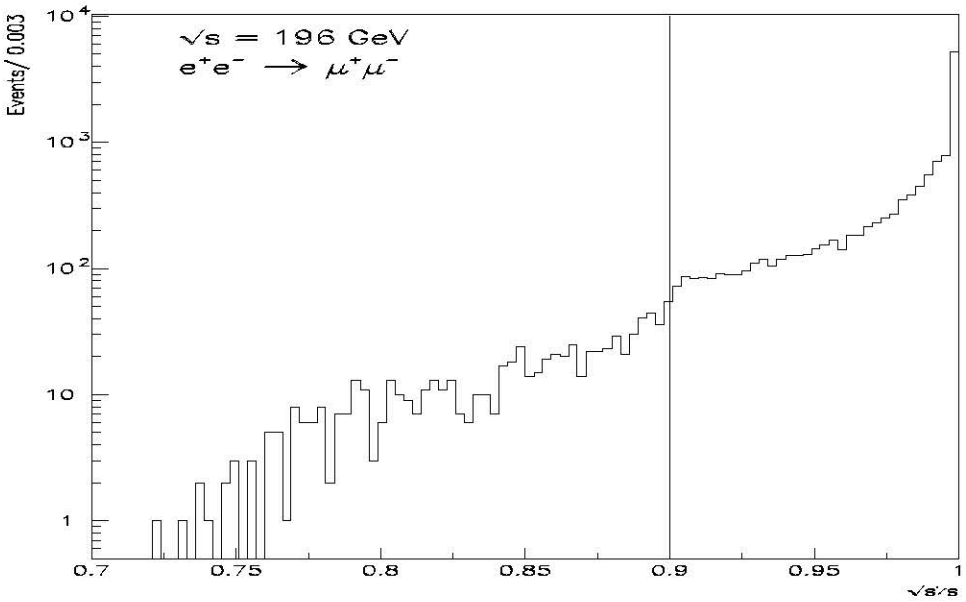

Figure 4.6:
The true $\sqrt{s'/s}$ is shown for events selected in the exclusive sample. Those with $\sqrt{s'/s} < 0.9$ are double radiative events and have to be subtracted as background.

$\sqrt{s'/s}$ cut	BG Channel	196 GeV	200 GeV	202 GeV
0.1	$\gamma\gamma \to \mu\mu$	3.7 ± 0.8	4.6 ± 0.9	4.6 ± 0.9
	$\tau\tau$	0.9 ± 0.1	0.9 ± 0.1	0.9 ± 0.1
	WW	2.7 ± 0.2	3.0 ± 0.2	3.0 ± 0.2
	ZZ	0.9 ± 0.0	1.0 ± 0.0	1.0 ± 0.0
	Zee	1.3 ± 0.3	1.4 ± 0.3	1.4 ± 0.3
	Total	**9.5 ± 0.9**	**11.0 ± 1.0**	**10.9 ± 1.0**
0.9	$\gamma\gamma \to \mu\mu$	—	0.4 ± 0.4	0.4 ± 0.4
	WW	0.1 ± 0.1	0.1 ± 0.0	0.1 ± 0.1
	ZZ	0.2 ± 0.0	0.1 ± 0.0	0.1 ± 0.0
	double rad.	4.2 ± 0.2	3.7 ± 0.2	4.5 ± 0.2
	Total	**4.5 ± 0.2**	**4.3 ± 0.4**	**5.1 ± 0.4**

Table 4.3:
Background contributions from different processes with combined statistical and systematical errors (numbers in %, relative to data). The dash indicates that no event was selected.

Chapter 5

Dimuon Cross-Section and A_{FB}

5.1 Cross Section Measurement

Once the number of events N is determined and the integrated luminosity $\int \mathcal{L}\,\mathrm{dt}$ is measured, the cross section can be calculated with the formula

$$\sigma = \frac{N}{\int \mathcal{L}\,\mathrm{dt}} \quad . \tag{5.1}$$

The distributions for the invariant mass M_{inv} and $\sqrt{s'/s}$ are shown in figure 5.1. One can see that the Z-return peak and the high energetic end are much sharper in $\sqrt{s'_m/s}$ compared to M_{inv}. Especially the muon pairs with a high invariant mass that are selected for the exclusive measurement gather in a region with $\sqrt{s'_m/s} > 0.98$.

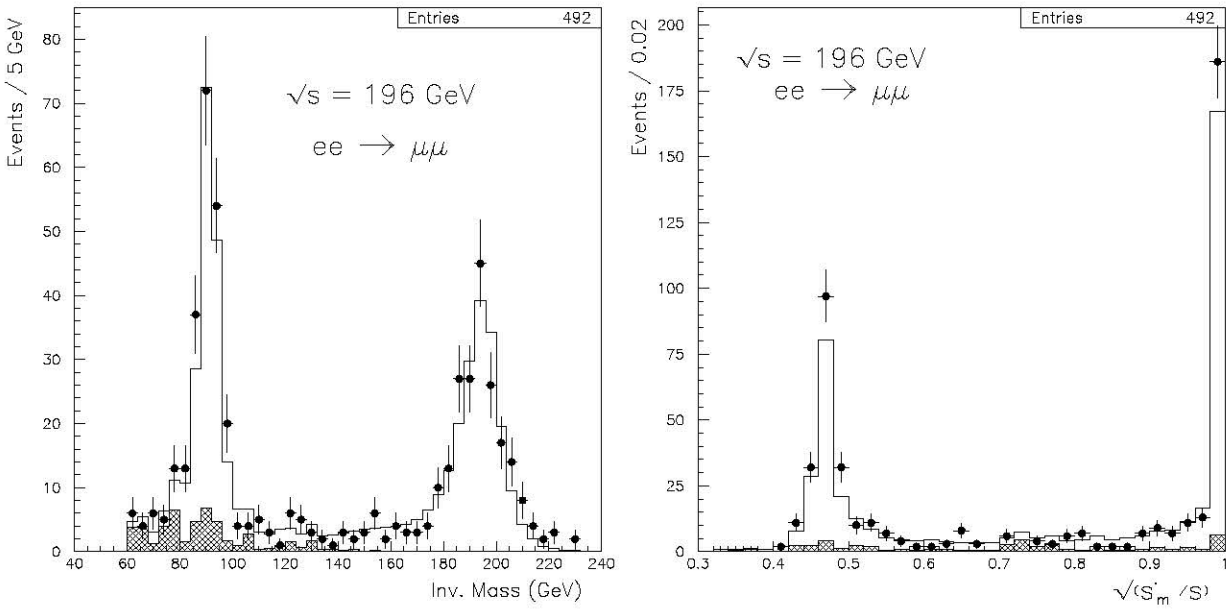

Figure 5.1:
Distributions of data (dots), signal MC (open histogram) and background (hatched histogram) in the variables invariant mass M_{inv} and $\sqrt{s'_m/s}$ for E_{CM} = 196 GeV.

The inclusive cross section, given for the range $\sqrt{s'/s} > 0.1$, includes events with hard ISR, a large part of the events in this sample being radiative Z-returns. This is visualized in figure 5.2, where the true $\sqrt{s'/s}$ is plotted versus the measured $\sqrt{s'_m/s}$. The diagonal shows events with single ISR while the accumulation of events at $\sqrt{s'_m/s} \approx 0.5$ shows radiative returns to the Z-peak. The horizontal band shows Z-returns with multiple ISR. Here only events with $|\cos\theta| < 0.95$ are shown as only those are accepted in the selection. Thus, an extrapolation on MC basis to the full solid angle has to be carried out to obtain the inclusive cross section.

The exclusive cross section is defined for a cut of $\sqrt{s'/s} > 0.9$; so the invariant mass of the dimuon pair is at least 90 % of the LEP centre-of-mass energy. The main background in this sample comes from double radiative events, where both positron and electron radiate a photon of approximately the same energy in the initial state. As described in section 4.4.3, these events might pass the $\sqrt{s'_m/s}$ cut, which is a cut on the acollinearity, because the muons are back-to-back. Figure 5.2 shows the cut for which the cross section is defined and the cut that is actually applied. A strict cut on the invariant mass is only applied at 150 GeV/c^2 and not at $0.9 \cdot \sqrt{s}$ as the momentum measurement is not as precise as the measurement of the angles and so the invariant mass distribution is smeared out. In order not to cut in the signal region, the contribution of double radiative events in the sample is estimated by MC simulations where the true invariant mass is known.

Luminosity Measurement

The luminosity is determined from low-angle Bhabha scattering where events with coincidental signals in the forward and backward part of LCAL are selected. It is calculated for each run as:

$$L = N/\frac{\sigma_0 s_0}{s} \tag{5.2}$$

where N is the number of selected Bhabha events, σ_0 and s_0 are the theoretical SM cross section calculated for the acceptance of LCAL and the centre-of-mass energy squared respectively and s is twice the LEP energy squared. L denotes that the integration over time is already carried out and is therefore equal to $\int \mathcal{L}\,dt$. The error on the integrated luminosity consists of a statistical part arising from the finite number of Bhabha events and a systematic part originating from theoretical uncertainties and detector effects. A more detailed description of the luminosity measurement can be found in reference [30]. The exact LEP energies and integrated luminosities with the statistical and systematic error used in the present analysis are given in table 5.1. A short account of the effects that cause the systematic error on the integrated luminosity is given in chapter 5.3.

Energy (GeV)	Integrated Luminosity(pb^{-1})
195.519	$79.834 \pm 0.141(stat) \pm 0.340(syst)$
199.516	$86.298 \pm 0.150(stat) \pm 0.367(syst)$
201.625	$41.991 \pm 0.106(stat) \pm 0.179(syst)$

Table 5.1:
Precise centre-of-mass energies and the corresponding recorded integrated luminosities with statistical and systematic errors used in the present analysis.

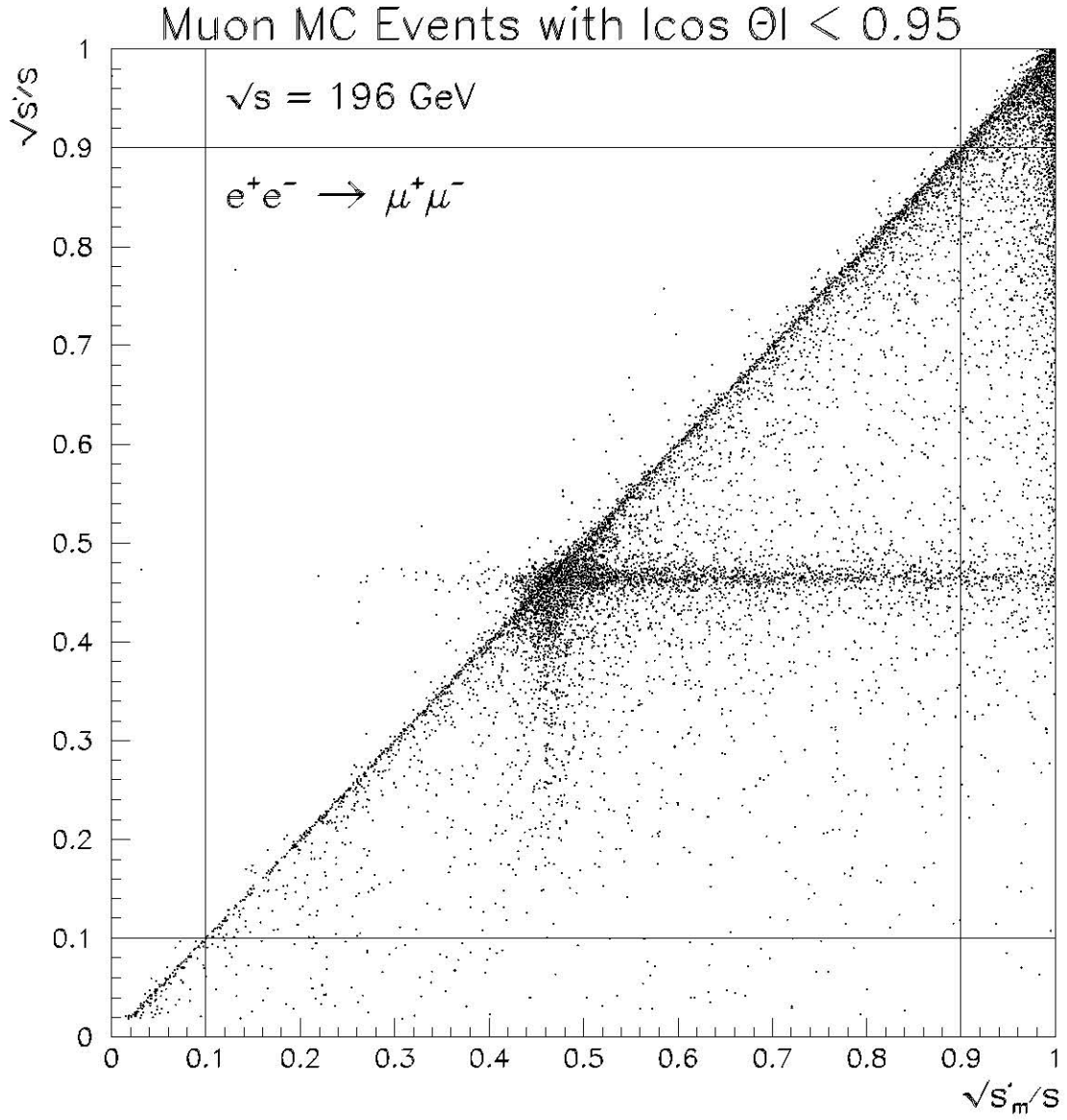

Figure 5.2:
True $\sqrt{s'/s}$ versus measured $\sqrt{s'_m/s}$ after detector simulation for dimuon events at 196 GeV. The diagonal shows events with single ISR while the accumulation of events at $\sqrt{s'_m/s} \approx 0.5$ shows radiative returns to the Z-peak. The horizontal band shows Z-returns with multiple ISR. The lines indicate the cuts applied for the inclusive and exclusive selection in the true and measured variables $\sqrt{s'/s}$ and $\sqrt{s'_m/s}$ respectively.

Background Subtraction and Efficiency Correction

From the selected events background events have to be subtracted. The contributions from different processes were determined from simulated events and normalized to the integrated luminosity of the data. The number of signal events is then defined as

$$N = (N^{Data} - \sum_i (w_i \, N_i^{BG})) \cdot \frac{1}{\epsilon'_\mu} \tag{5.3}$$

with N^{Data} being the number of selected events, the sum running over all the backgrounds i and the w_i being the weight factors depending on the amount of generated events and the cross section for the particular process. The weight factors are in detail:

$$w_i = L^{Data}/L^{MC} = \frac{L^{Data}}{N_i^{genMC}/\sigma_i} \tag{5.4}$$

Now the remaining number of events still has to be corrected for the selection efficiency ϵ'_μ for the signal, which also takes into account the background contribution from double radiative events in the exclusive selection.
The selection efficiency is determined by comparing events at generator level and after detector simulation. In this case the critical questions are: Are the various observables reconstructed in the proper way and how often do mismeasurements occur? As both, the inclusive and exclusive process, are only defined for particular regions of phase space, each event can be assigned to one out of four event classes:

- N_{sel}^{true} is the number of events that pass the selection cuts on the generator ($true$) and the detector (sel) level
- $N_{sel}^{not\ true}$ is the number of events that do not pass the cuts at the generator level but at the detector level (e.g. double radiative events)
- $N_{not\ sel}^{true}$ is the number of events that pass the cuts at the generator level but do not pass them at the detector level
- $N_{not\ sel}^{not\ true}$ is the number of events that pass the cuts neither at the generator nor at the detector level

Since there are four different possible outcomes when an event is generated, one is dealing with a multinomial distribution. The four event classes are not independent from each other but correlated. Therefore when one is calculating the error on a combination of numbers from different classes, these correlations have to be taken into account by using the proper covariance matrix. The entries of this matrix are defined as

$$V_{ij} = -\frac{N_i N_j}{N} \qquad \text{for } i \neq j, \tag{5.5}$$

otherwise

$$V_{ii} = N_i(1 - \frac{N_i}{N}) \qquad \text{for } i = j. \tag{5.6}$$

The selection efficiency is now the ratio between the total number of selected events and the total number of true events:

$$\epsilon'_\mu = \frac{N_{sel}^{true} + N_{sel}^{not\ true}}{N_{sel}^{true} + N_{not\ sel}^{true}} \tag{5.7}$$

The value of this number can be larger than one. This is the case when $N_{sel}^{not\ true} > N_{not\ sel}^{true}$, meaning that more events that do not fulfill the selection criteria on the generator level are reconstructed to be true than the other way round. An example of this is the exclusive selection, in which double radiative events pass the applied cuts.

At this stage all the numbers that are needed to calculate the cross section are determined:

$$\sigma_{\mu\mu} = \frac{N}{L} = \frac{N^{Data} - N_{tot}^{BG}}{L} \frac{1}{\epsilon'_{\mu}} \tag{5.8}$$

The cross section $\sigma_{\mu\mu}$ is thus a function of six variables $\vec{x} = (N^{Data}, N_{tot}^{BG}, L, N_{sel}^{true}, N_{not\ sel}^{true}, N_{sel}^{not\ true})$, the latter three being correlated. In this case the variance of the cross section $\sigma_{\mu\mu}$ has to be calculated as:

$$V[\sigma_{\mu\mu}(\vec{x})] = \sum_{i,j=1}^{6} \left[\frac{\partial \sigma_{\mu\mu}}{\partial x_i} \frac{\partial \sigma_{\mu\mu}}{\partial x_j} \right] V_{ij} \tag{5.9}$$

with the V_{ii} and V_{ij} being the corresponding variances and covariances of the x_i.

The cross sections measured with this method are given in table 5.2 together with SM predictions obtained from ZFITTER (v6.23) [15]. None of them shows significant deviations from SM predictions, indeed most agree within the 1 σ statistical error. Figure 5.3 a) summarizes all the inclusive and exclusive cross sections measured by ALEPH from $130 - 192\ GeV$ [22, 31, 32] and the results of this analysis at $196 - 202\ GeV$.

$\sqrt{s'/s}$ cut	E_{CM} (GeV)	No. of Events	$\sigma_{\mu\mu}$ (pb)	SM prediction (pb)
0.1	195.519	492	$7.565 \pm 0.376(stat) \pm 0.083(syst)$	7.105
	199.516	489	$6.834 \pm 0.347(stat) \pm 0.086(syst)$	6.790
	201.625	238	$6.914 \pm 0.502(stat) \pm 0.087(syst)$	6.634
0.9	195.519	206	$2.567 \pm 0.179(stat) \pm 0.021(syst)$	2.463
	199.516	244	$2.798 \pm 0.180(stat) \pm 0.029(syst)$	2.355
	201.625	106	$2.487 \pm 0.242(stat) \pm 0.023(syst)$	2.300

Table 5.2:
Measured inclusive and exclusive cross sections together with statistical and systematic errors. In the last column the SM predictions are given for comparison.

5.2 Measurement of the Dimuon Asymmetry

In e^+e^- – collisions the production of muon pairs can either be mediated by a γ or through the exchange of a Z-boson. The interference between the two diagrams leads to a term which is responsible for an asymmetric angular distribution of the final state leptons. This means that the μ^- is scattered more often in the direction of the incoming e^-. The differential cross section with respect to θ^* is given in eq. 2.13. Since the asymmetry is a function of E_{CM},

which is shown by the solid line in figure 5.3 b), it is only determined for the exclusive sample as already mentioned in section 2.2.

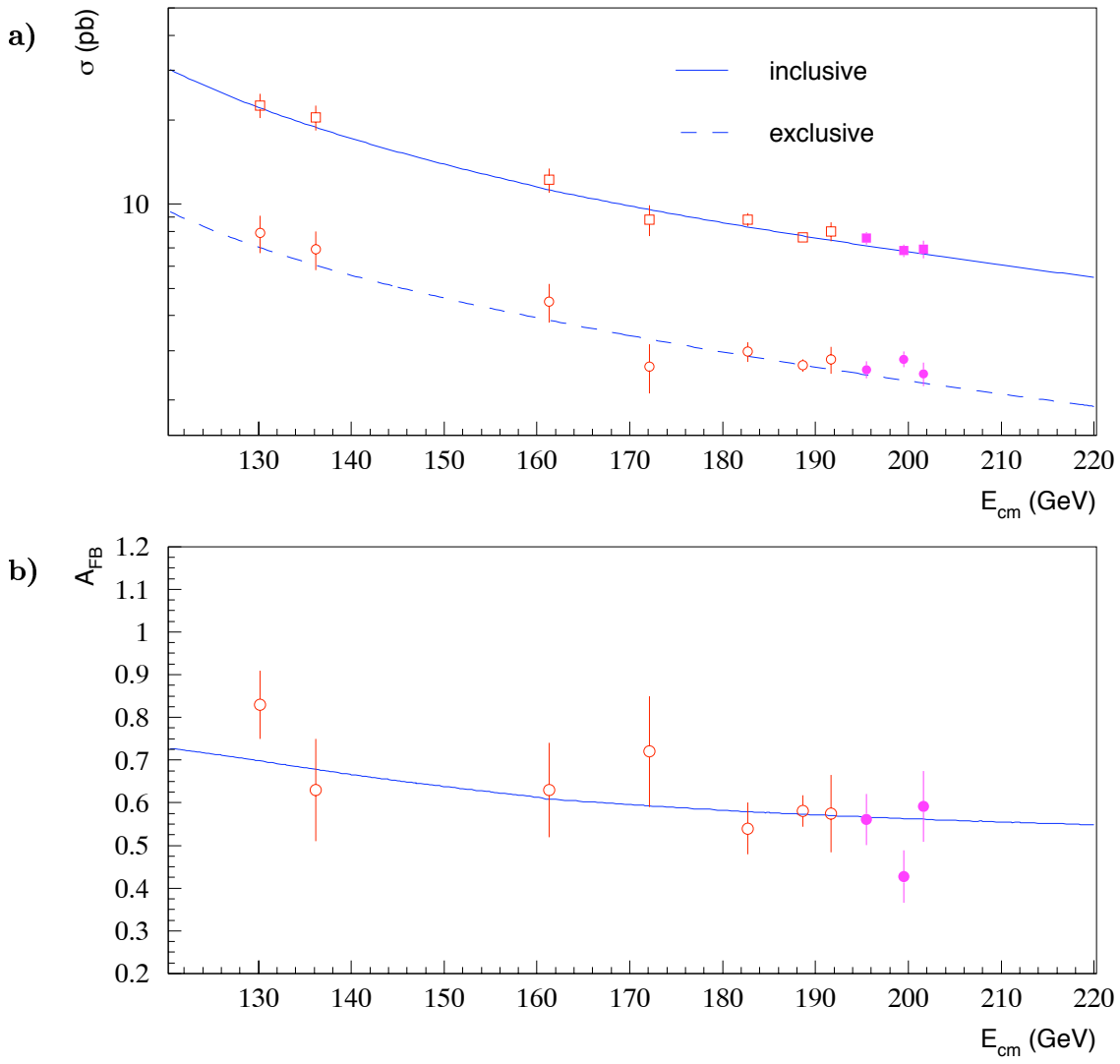

Figure 5.3:
In figure a) the official inclusive (open squares) and exclusive (open circles) cross section measurements of ALEPH at centre-of-mass energies from $130-192$ *GeV are shown. The full squares and circles show the values obtained with the present analysis at energies from* $196-202$ *GeV. Figure b) shows the results of the forward-backward asymmetry measurements (open circles: official ALEPH results; full circles: results of this analysis). The curves indicate the expected cross sections and asymmetries from ZFITTER.*

Of course this asymmetry has to be measured in the $\mu^+\mu^-$ rest frame, which in this case is approximately equal to the detector frame because only soft ISR photons are allowed in the exclusive sample. For this reason the invariant mass of the muon pair is roughly the same as

twice the LEP energy. The scattering angle θ^* in the $\mu^+\mu^-$ rest frame can be calculated with eq. 2.15. Figure 5.4 demonstrates this strong dependence of $\cos\theta^*$ on $\cos\theta$ for MC and data at 196 GeV. One can also see that this correlation is not so strong for the inclusive sample. The events on the fringes are Z-returns with one hard ISR photon. This means that the events get boosted and consequently $\cos\theta^*$ and $\cos\theta$ are not the same anymore.

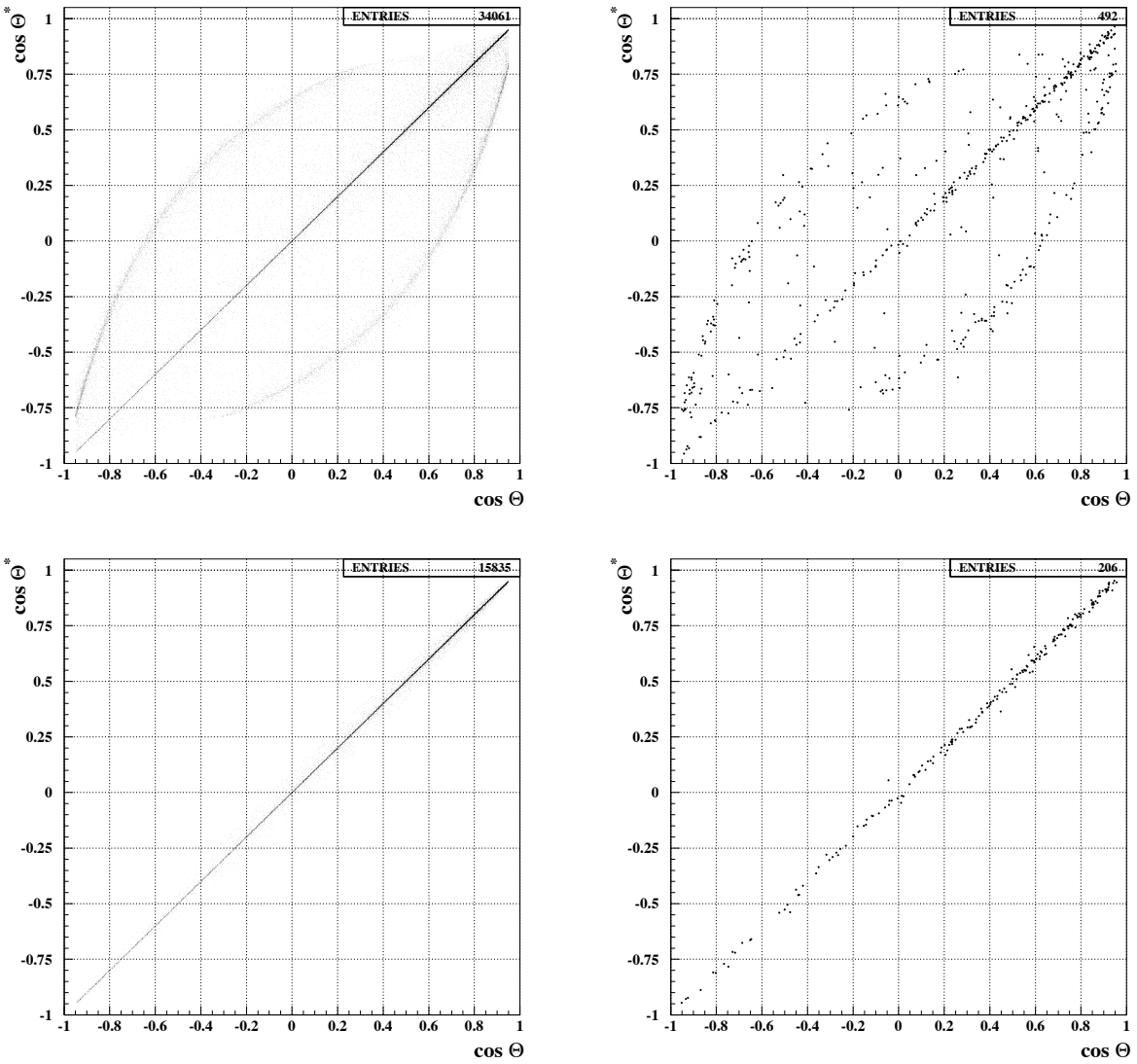

Figure 5.4:
Dependence of $\cos\theta^*$ *on* $\cos\theta$ *for* $\sqrt{s'/s} > 0.1$ *and* $\sqrt{s'/s} > 0.9$ *at 196 GeV. The upper left diagram shows MC simulation for the inclusive sample while in the upper right the data is shown. Events on the bent fringes are boosted Z-returns. The two diagrams at the bottom show MC on the left and data on the right for the exclusive sample. As expected,* $\cos\theta$ *and* $\cos\theta^*$ *are strongly correlated in this case since only soft ISR photons are allowed. This means as well that the laboratory frame and the rest frame of the* $\mu^+\mu^-$ *system are approximately the same.*

The angular distributions of data, MC predictions for signal and background are shown in figure 5.5. Here the forward-backward asymmetry is clearly visible.

The forward-backward asymmetry A_{FB} is defined as the difference of the cross sections σ_i in the forward ($\cos\theta^* > 0$) and backward ($\cos\theta^* < 0$) direction relative to the total cross section (see eq. 2.12), which is equal to the difference in the observed events N_i relative to the total number of events:

$$A_{FB} = \frac{N_F - N_B}{N_F + N_B} \tag{5.10}$$

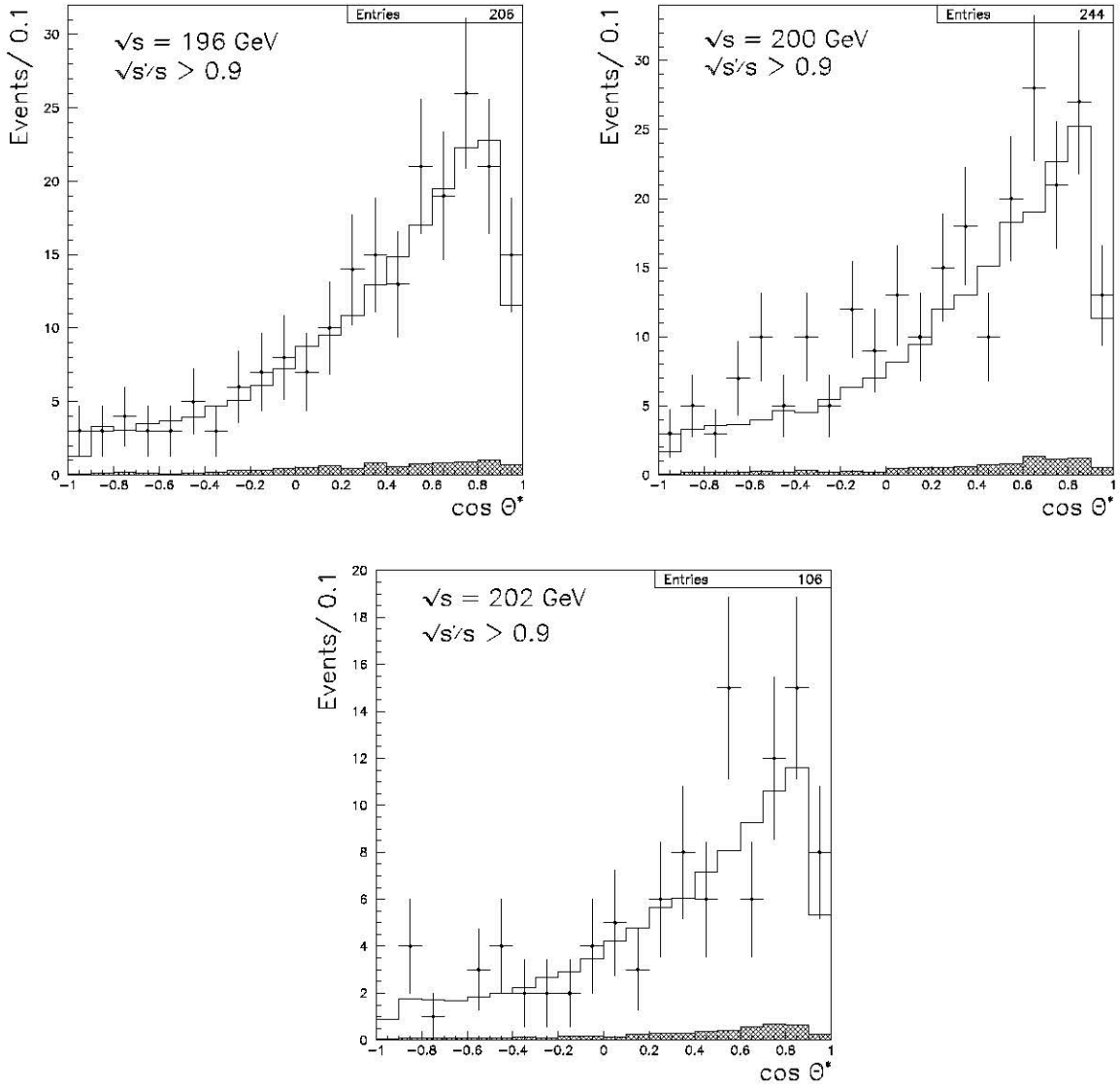

Figure 5.5:
Distribution of $\cos\theta^*$ for dimuon events at energies of 196, 200 and 202 GeV. Dots are the data with statistical error, the white histogram represents the MC estimation and the grey histogram indicates the expected background.

The forward-backward asymmetry is therefore simply determined by counting the number of events in the forward and backward direction. The $\cos\theta^*$ range is divided into 20 bins of equal width and for each bin a selection efficiency is determined on the basis of MC simulations. In this case the efficiency is defined as the number of selected events divided by the number of generated events in each bin.

The main background originates from double radiative events and their fraction is determined with the help of the MC truth information. The contributions from other processes are very small as can be seen from table 4.3. The angular distribution of this background is assumed to be flat since it has no statistical significance with the limited number of MC events used and so its contributions were averaged over all the bins. Therefore it cancels out in the numerator in eq. 5.10 but has to be subtracted from the total number of events in the denominator. The number of events in each bin i was then determined by

$$N_i = (N_i^{data} - w_\mu N_i^{2rad})\frac{1}{\epsilon_i} \quad . \tag{5.11}$$

This number N_i is a function of four variables $\vec{x} = (N_i^{data}, w_\mu, N_i^{2rad}, \epsilon_i)$ which were treated as not correlated and hence the error on it was calculated as

$$\delta N_i = \sqrt{\sum_{j=1}^{4} \left(\frac{\partial N_i}{\partial x_j}\right)^2 (\delta x_j)^2} \quad . \tag{5.12}$$

Here a binomial error on the efficiencies ϵ_i was used. The error on N_F and N_B was obtained by summing quadratically over the bins in the forward and backward direction respectively. The total error on A_{FB} was determined as

$$\delta A_{FB} = \frac{2}{(N_F + N_B)^2}\sqrt{(N_B\ \delta N_F)^2 + (N_F\ \delta N_B)^2} \quad . \tag{5.13}$$

The forward-backward asymmetries measured with this method are given in table 5.3 together with the SM predictions obtained from ZFITTER. The asymmetries at 196 GeV and 202 GeV agree well with the SM values while the one at 200 GeV is about 2.3 standard deviations too low. This is still compatible with a statistical fluctuation. Figure 5.3 summarizes all the asymmetries for muon pairs measured by ALEPH at energies from $130 - 192\ GeV$ [22, 31, 32] and the results of this analysis at $196 - 202\ GeV$ with statistical errors. The solid line gives the ZFITTER prediction for the forward-backward asymmetry. One can see that all the measurements agree with the theoretical predictions.

5.3 Systematic Errors and Corrections

Apart from statistical errors also systematic errors have to be taken into account. They arise for example from uncertainties in the theoretical predictions or from errors on physical quantities that enter the analysis but have to be measured experimentally as well. In the following section the sources for systematic errors shall be discussed. The results are summarized in table 5.7 at the end of this section.

Energy (GeV)	A_{FB}	SM prediction
195.519	$0.561 \pm 0.060(stat) \pm 0.002(syst)$	0.567
199.516	$0.427 \pm 0.061(stat) \pm 0.003(syst)$	0.563
201.625	$0.591 \pm 0.083(stat) \pm 0.002(syst)$	0.561

Table 5.3:
Muon forward-backward asymmetry with statistical and systematic errors measured for $\sqrt{s'/s} > 0.9$ *and* $|\cos\theta| < 0.95$. *The SM predictions are calculated with ZFITTER including ISR/FSR interference.*

Luminosity uncertainties

The error on the luminosity consists of two parts, a statistical and again a systematic one. As the luminosity is calculated from the number of Bhabha events that are recorded in LCAL, it obviously has a statistical uncertainty. But as it is a measured quantity, there is also a contribution arising from systematic effects. The dominating part originates from the definition of the geometrical acceptance. Here it is the internal mechanical precision of the calorimeter and the precision on the fiducial cut that give the major contributions [30, 33]. Limited MC statistics for Bhabha events and uncertainties in the theoretical predictions provide another source for systematic uncertainties on the luminosity. All the systematic effects considered for the luminosity measurement at the analysed centre-of-mass energies are given in [30] and sum up to a total systematic error of 0.41% on the integrated luminosity L. For all the data samples that are used in this analysis the systematic error dominates the total error on L.

Limited background MC statistics

Another systematic effect arises from the finite number of simulated MC events that are used. As the number of generated events is a multiple of the events seen in the data, it also corresponds to a different luminosity. Therefore a selected MC event has to be weighted with a factor w_i according to the ratio of the luminosities of data and MC given by eq. 5.4 which depends on the number of generated events and the predicted cross section. As the MC cross section is calculated on the basis of generated events, its precision depends on the total number of produced events and therefore it has a statistical error. Additionally, a MC generator only considers contributions from higher order diagrams up to a certain order which results in an uncertainty on the cross section. For the processes $e^+e^- \to ZZ$ and Ze^+e^-, generated by PYTHIA, an error of 2 % and 20 % respectively was assumed [34]. KORALW is used to produce W-pair events but as this cross section is normalized to the GENTLE [35] value, the 2 % error on the prediction from the latter was applied [36].

When subtracting the weighted number of background events from the selected data events (see eq. 5.3), one introduces a systematic error as both the weight factor w_i and the number of events N_i^{BG} are afflicted with an error. The error on the weight factor w_i is calculated as

$$\delta w_i = \frac{L^{Data}}{N_i^{genMC}} \, \delta\sigma_i^{MC} \tag{5.14}$$

with no errors being assigned to N^{genMC} because it is a precise and arbitrary number and L^{Data} as it drops out in the calculation of the cross section. The error on the number of selected background events is binomial and so

$$\delta N_i^{BG} = \sqrt{N_i^{BG}\left(1 - \frac{N_i^{BG}}{N^{genMC}}\right)} \quad . \tag{5.15}$$

Finally, the total error on the weighted subtracted background is taken as a systematic error coming from background MC simulations.

As already discussed in section 4.4.1 an additional systematic error is applied to the background originating from $e^+e^- \to \gamma\gamma$ because the MC prediction exceeds the number of events seen in the data in a region where this process is dominant (see figure 4.5). Since this excess is stable over the whole range of M_{inv} in the window between 20 - 60 GeV and over all the three energies, the $e^+e^- \to \gamma\gamma$ cross section was corrected. As the correction factor the weighted average of the excess at the three energy points was taken and its error was included as a systematic uncertainty on this background. The results are given in table 5.4. At this point it is probably appropriate to mention that for 200 GeV and 202 GeV the same MC sample was used. However, this does not cause any problems since the $e^+e^- \to \gamma\gamma$ cross section is varying very slowly with energy in this range.

Energy (GeV)	$\frac{(\sum_i N_i^{MC}) - N^{Data}}{N_{\gamma\gamma}^{MC}}$
196	0.163 ± 0.067
200	0.182 ± 0.064
202	0.187 ± 0.078
weighted average	0.177 ± 0.040

Table 5.4:
Correction factors and errors on the $e^+e^- \to \gamma\gamma$ MC background for different E_{CM}. The overall weighted average was taken as a systematic correction to the $e^+e^- \to \gamma\gamma$ background contribution while the error on this factor was included in the systematic error.

Statistical error due to signal MC

Systematic uncertainties are not only caused by background MC but arise also from signal MC. The muon MC is used to calculate the efficiency and therefore the uncertainties are caused by the limited number of events and the correlations between the different event classes defined in 5.1. Its contribution can be calculated by using equation 5.9 with the index i running from 4 - 6.

Muon pair identification using Z-peak data

A comparison of data and MC at the Z-peak can be used to determine the muon identification efficiency. This factor is a systematic correction on the selection efficiency determined from

the signal MC and contributes an additional systematic error on the latter. A data sample with $E_{CM} = m_Z \cdot c^2$ was taken at the beginning of the run period with the same detector configuration as at high energies. Since muons are always produced in pairs at the Z-peak, one can verify the muon identification efficiency with real data. This is done by comparing the number of events where one muon is identified N_1 with the number of events, where two muons are identified N_2 in a region of phase space where only dimuon events are expected. In order to verify this assumption, the whole procedure is applied to both data and muon MC. At the Z-peak a data sample with an integrated luminosity of $3,46\ pb^{-1}$ was taken, resulting in $\approx$ 4000 selected muon events. 30000 MC events were simulated out of which $\approx$ 22000 passed the selection.

The cuts used to obtain a data sample of muons with high purity were the following:

- the sum of the momenta of the two muons has to exceed 85 GeV and has to be less than 100 GeV
- the maximum of the energy deposited in ECAL by one of the muons has to be less than 2.5 GeV
- the acollinearity has to be less than 0.1
- the sum of the charges of the two tracks has to be zero

The efficiency to identify a single muon in an event is given by

$$\epsilon_{\mu_{id}} = \frac{2N_2}{N_1 + N_2} \tag{5.16}$$

and consequently, the probability to identify two muons in an event is given by $(\epsilon_{\mu_{id}})^2$. The ratio of the efficiencies in data $(\epsilon_{\mu_{id}}^{Data})^2$ and MC $(\epsilon_{\mu_{id}}^{MC})^2$ is applied as a correction factor to the cross section. The efficiencies for muon identification in data and MC are summarized in table 5.5. The cross section was corrected by the factor in the last column and the error on it included in the systematic error.

Z-peak sample	$(\epsilon_{\mu_{id}}^{Data})^2$	$(\epsilon_{\mu_{id}}^{MC})^2$	$(\epsilon_{\mu_{id}}^{MC}/\epsilon_{\mu_{id}}^{Data})^2$
1999	0.9548 $\pm$ 0.0024	0.9583 $\pm$ 0.0010	1.0037 $\pm$ 0.0027

Table 5.5:
Efficiencies for muon identification obtained from data and MC at the Z-peak. In the last column the overall correction factor to the cross section is given.

Efficiency correction for exact E_{LEP}

Another systematic effect arises from the fact that the MC files are produced at the nominal and not at the real LEP energy. This is of importance since the selection efficiency is a function of $\sqrt{s'/s}$. At higher centre-of-mass energies, the Z-return peak and the peak of the events at E_{CM} get more and more separated in M_{inv} and $\sqrt{s'/s}$ (see figure 5.1 for

illustration). In consequence, the shape of the MC prediction is not exactly correct if the nominal and real E_{LEP} differ and this affects the selection efficiency. The selection efficiency as a function of $\sqrt{s}$ can be calculated as

$$\epsilon(\sqrt{s}) = \frac{1}{\sigma^{tot}_{\mu\mu}(s)} \sum_{bins\ j} \left(\int \frac{\partial \sigma_{\mu\mu}(s)}{\partial x} dx \right)_j \epsilon^{MC}_j \tag{5.17}$$

with $x = \sqrt{s'/s}$ and the bins j in $\sqrt{s'/s}$ running from 0.1 to 1.0 with a width of 0.05. As one can see, for each bin the MC efficiencies are weighted with the integrated differential cross sections calculated with ZFITTER and then normalized to the total cross section $\sigma^{tot}_{\mu\mu}$ obtained from ZFITTER as well. This weighting procedure is carried out twice, once for the nominal and once for the real LEP energy. The overall correction factor η_{corr} is then obtained by taking the ratio of the two efficiencies,

$$\eta_{corr} = \frac{\epsilon(E^{\ nominal}_{CM})}{\epsilon(E^{\ real}_{CM})} \quad . \tag{5.18}$$

The correction factors are given in table 5.6, where the errors have been neglected as they are negligibly small. The whole procedure can be omitted for the exclusive cross section as in that case almost all events are in the last bin of $\sqrt{s'/s}$ and therefore no change in the efficiency is expected (see figure 5.1).

Energy (GeV)	η_{corr}
$196 \rightarrow 195.519$	0.9988
$200 \rightarrow 199.516$	0.9978
$202 \rightarrow 201.625$	0.9981

Table 5.6:
Correction factors for the inclusive cross section arising from the fact that the signal MC was produced at the nominal and not at the real LEP energy.

The contributions from all the investigated systematic sources are listed in table 5.7. The systematic errors add up to about 1 % of the total cross section value but as one can see from table 5.2, they are small compared to the statistical error, which is about 5 %.

$\sqrt{s'/s}$ cut	Source of Error	E_{CM} 196 GeV	200 GeV	202 GeV
0.1	Luminosity	0.4	0.4	0.5
	Background MC	1.0	1.1	1.1
	Signal MC	0.1	0.2	0.1
	Muon identification	0.3	0.3	0.3
	Total	**1.1**	**1.3**	**1.3**
0.9	Luminosity	0.4	0.4	0.5
	Background MC	0.1	0.4	0.4
	Signal MC	0.6	0.8	0.6
	Muon identification	0.3	0.3	0.3
	Total	**0.8**	**1.0**	**0.9**

Table 5.7:
Summary of systematic errors for the inclusive and exclusive cross section measurement. All numbers given are in %.

Chapter 6

New Physics

> A plausible impossibility is always preferable to an unconvincing possibility.
>
> Aristotle, Poetics, 24

Although the predictions based on the SM are very successful, especially the precision measurements of electroweak observables, it cannot provide answers to all questions, e.g. the breakdown of the electroweak symmetry or the hierarchy problem. For these reasons several extensions to the SM have been developed and two of these shall be discussed in this chapter, namely Contact Interactions and TeV-Scale Quantum Gravity.

As already mentioned in chapter 2.3, the general concept is to add extra terms to the SM-Lagrangian, representing new particles or interactions which change the total cross sections and angular distributions.

As input data the measured exclusive cross sections and angular distributions by ALEPH at centre-of-mass energies between 130 GeV and 202 GeV for all the two-fermion processes have been used [22, 32, 31]. Maximum likelihood fits to cross section and angular distribution have been carried out for the dimuon and ditau data while for the Bhabha channel only the angular distribution was fitted. In the case of the $q\bar{q}$ channel the angular distribution was fitted and the charge asymmetry Q_{FB}, the latter only for the 183 GeV and 189 GeV data. The theoretical errors assumed on the SM predictions obtained from ZFITTER are summarized in table 6.1. A decrease of the theoretical errors would result in higher limits for beyond SM processes. Thus more precise calculations are needed.

6.1 Limits on Four Fermion Contact Interactions

As the 'elementary particles' became more and more elementary with the progress of science and new methods to probe the constituents of matter, a natural extension of the SM is to look for composite structures in quarks and leptons. If fermions have a substructure and are bound states of more fundamental constituents (often called preons [37]), new effective interactions among them should arise. These Contact Interactions should occur at a mass scale Λ that characterizes the strength of the new interaction and the physical size of the composite states [38]. The problem is approached by adding an extra term of a point-like

Channel	$\frac{\Delta\sigma^{SM}}{\sigma^{SM}}$ (%)	$\frac{\Delta A_{FB}^{SM}}{A_{FB}^{SM}}$ (%)
Hadrons	1.5	2.5
e^+e^-	2.5	—
$\tau^+\tau^-$	2.0	4.5
$\mu^+\mu^-$	2.0	9.0

Table 6.1:
Relative theoretical errors assumed for ZFITTER SM predictions on σ and A_{FB} (in %). The Bhabha forward-backward asymmetry was not fitted and in the hadronic case the charge-asymmetry Q_{FB} was used at input for the 183 GeV and 189 GeV data.

interaction (similar to Fermi's description of β-decay) to the SM-Lagrangian [39] of the form

$$\mathcal{L}^{CI} = \frac{g^2\eta_{sign}}{(1+\delta_{ef})\Lambda^2} \sum_{i,j=L,R} \eta_{ij}[\bar{e}_i\gamma^\mu e_i][\bar{f}_j\gamma_\mu f_j] \quad , \tag{6.1}$$

with $\delta_{ef} = 1$ if the fermion is an electron and 0 otherwise. The fields $e_{L,R}$ ($f_{L,R}$) are the left- and right-handed chirality projections of electron (fermion) spinors and the parameters η_{ij} determine the type of chiral coupling of the four fermions. The sign of η_{sign} denotes positive and negative interference with SM amplitudes respectively. By convention the coupling strength is set to $g = \sqrt{4\pi}$ and so Λ is a mass scale for a new exchange particle.

The analysis carried out here follows a procedure described in [22], where more details can be found. Several models for the chiral couplings and the effect of η_{sign} have been considered and are summarized in table 6.2.

Model	η_{sign}	η_{LL}	η_{RR}	η_{LR}	η_{RL}
$\mathrm{LL}^{\pm}$	±1	1	0	0	0
$\mathrm{RR}^{\pm}$	±1	0	1	0	0
$\mathrm{VV}^{\pm}$	±1	1	1	1	1
$\mathrm{AA}^{\pm}$	±1	1	1	-1	-1
$\mathrm{LR}^{\pm}$	±1	0	0	1	0
$\mathrm{RL}^{\pm}$	±1	0	0	0	1
$\mathrm{LL{+}RR}^{\pm}$	±1	1	1	0	0
$\mathrm{LR{+}RL}^{\pm}$	±1	0	0	1	1

Table 6.2:
Four-fermion interaction models. The η_{ij} represent the different chiral couplings while η_{sign} indicates constructive or destructive interference with the SM amplitudes.

The cross section for the SM and the Contact Interaction term was calculated in the improved Born approximation including the interference term and corrected for ISR according to [40]. The Born level formula for the differential cross section can be found in [39] and

appendix A.1. A binned maximum likelihood was used to fit the predictions of eq. 6.2 to the data.

$$\frac{d\sigma}{d\cos\theta} = F_{\mathrm{SM}}(s,t)\left[1 + \epsilon\frac{F_{\mathrm{IF}}^{\mathrm{Born}}(s,t)}{F_{\mathrm{SM}}^{\mathrm{Born}}(s,t)} + \epsilon^2\frac{F_{\mathrm{CI}}^{\mathrm{Born}}(s,t)}{F_{\mathrm{SM}}^{\mathrm{Born}}(s,t)}\right] \tag{6.2}$$

$F_{\mathrm{SM}}(s,t)$ (with s and t being the Mandelstam variables) is the SM cross section calculated with BHWIDE [26] for the e^+e^- channel and ZFITTER [15] for all others while $F_{\mathrm{IF}}^{\mathrm{Born}}(s,t)$ and $F_{\mathrm{CI}}^{\mathrm{Born}}(s,t)$ represent the contributions from the interference term and the pure Contact Interaction term respectively. The ratios of these were taken as no higher order predictions are available for the Contact Interactions. The number of data events, the number of predicted events and the systematic uncertainties on the expected events together with the parameter ϵ were fitted. As can be seen from eq. 6.2, the parameter ϵ is a measure of the deviation from the SM, where a value of $\epsilon = 0$ means that no deviation is observed. The parameter ϵ, the mass scale Λ and the coupling g are connected via the relationship

$$\epsilon = \frac{\eta_{sign} g^2}{4\pi\Lambda^2} \quad . \tag{6.3}$$

Since the theoretical cross sections depend quadratically on ϵ, the likelihood function can have two maxima. For this reason the 68 % confidence level limits on ϵ are calculated in the following way:

$$\int_{-\infty}^{\epsilon^-} \mathcal{L}(\epsilon')d\epsilon' = \int_{\epsilon^+}^{\infty} \mathcal{L}(\epsilon')d\epsilon' = 0.16\int_{-\infty}^{\infty} \mathcal{L}(\epsilon')d\epsilon' \tag{6.4}$$

With this method one avoids to take the 1 σ error from a central value that is eventually not connected with a maximum of the likelihood function. As already mentioned, ϵ is a measure for deviations from the SM and from eq. 6.2 it becomes clear that for positive values of ϵ the interference of the Contact Interactions with the SM is constructive while for negative values it is destructive. Additionally, limits on the mass scale Λ can be derived from ϵ with the help of eq. 6.3. The 95 % confidence level limits on $\epsilon_{95}^{\pm}$ were calculated in a different way:

$$\int_0^{\epsilon_{95}^+} \mathcal{L}(\epsilon')d\epsilon' = 0.95\int_0^{\infty} \mathcal{L}(\epsilon')d\epsilon' \ , \qquad \int_{\epsilon_{95}^-}^{0} \mathcal{L}(\epsilon')d\epsilon' = 0.95\int_{-\infty}^{0} \mathcal{L}(\epsilon')d\epsilon' \tag{6.5}$$

Here the likelihood function was integrated from $0 \to \pm\infty$ and 95 % of the halfsided integral respectively. By assuming a coupling of $g = \sqrt{4\pi}$ two values for Λ can be calculated from the positive and negative values of $\epsilon_{95}^{\pm}$ according to

$$\Lambda_{95}^{\pm} = 1 \Big/ \sqrt{|\epsilon_{95}^{\pm}|} \ . \tag{6.6}$$

Here the + and − signs on $\Lambda_{95}^{\pm}$ simply denote that the limits are calculated from the corresponding value of $\epsilon_{95}^{\pm}$ and have no physical meaning in terms of different couplings. The results for the 68 % confidence level limits on ϵ^+ and ϵ^- as well as the 95 % confidence level limits on Λ_{95}^+ and Λ_{95}^- are presented in table 6.3 for leptonic final states. In table 6.4 the results for Contact Interactions affecting the hadronic channel and all difermion channels combined are given. One can see that the limits derived for the different models are all of the order of 5 - 10 TeV.

Contact Term Fits (130 - 202 GeV)

Model	$[\epsilon^-,\epsilon^+]$ (TeV^{-2})	Λ^-_{95} (TeV)	Λ^+_{95} (TeV)
$e^+e^- \to e^+e^-$			
LL	$[-0.038, +0.087]$	5.1	3.4
RR	$[-0.039, +0.090]$	5.1	3.3
VV	$[-0.009, +0.018]$	10.4	7.5
AA	$[-0.017, +0.014]$	7.8	8.4
LR	$[-0.024, +0.050]$	6.4	4.5
LL+RR	$[-0.020, +0.044]$	7.0	4.8
LR+RL	$[-0.013, +0.020]$	8.9	7.0
$e^+e^- \to \mu^+\mu^-$			
LL	$[-0.016, +0.041]$	8.0	5.0
RR	$[-0.017, +0.044]$	7.6	4.8
VV	$[-0.005, +0.017]$	13.7	7.6
AA	$[-0.011, +0.015]$	9.5	8.1
LR	$[-0.289, +0.059]$	1.9	4.1
LL+RR	$[-0.008, +0.022]$	11.1	6.8
LR+RL	$[-0.264, +0.033]$	1.9	5.5
$e^+e^- \to \tau^+\tau^-$			
LL	$[-0.049, +0.022]$	4.5	6.7
RR	$[-0.055, +0.024]$	4.3	6.5
VV	$[-0.017, +0.009]$	7.6	10.7
AA	$[-0.026, +0.015]$	6.2	8.2
LR	$[-0.249, +0.046]$	2.0	4.7
LL+RR	$[-0.024, +0.012]$	6.4	9.2
LR+RL	$[-0.242, +0.026]$	2.0	6.3
$e^+e^- \to l^+l^-$			
LL	$[-0.016, +0.029]$	8.0	5.9
RR	$[-0.017, +0.031]$	7.7	5.7
VV	$[-0.005, +0.011]$	14.4	9.7
AA	$[-0.010, +0.009]$	10.2	10.3
LR	$[-0.017, +0.036]$	7.6	5.3
LL+RR	$[-0.008, +0.015]$	11.1	8.1
LR+RL	$[-0.009, +0.017]$	10.8	7.7

Table 6.3:
Results of contact interaction fits to leptons based on all LEP2 measurements. The 68% confidence level range is given for ϵ whilst the 95% confidence level limits are given for Λ. The results presented for l^+l^- assume lepton universality.

Contact Term Fits (130 - 202 GeV)

Model	$[\epsilon^-,\epsilon^+]$ (TeV^{-2})	Λ^-_{95} (TeV)	Λ^+_{95} (TeV)
$e^+e^- \to q\bar{q}$			
LL	$[-0.015, +0.021]$	8.2	6.9
RR	$[-0.045, +0.040]$	4.7	5.0
VV	$[-0.017, +0.014]$	7.7	8.4
AA	$[-0.008, +0.012]$	11.1	9.2
LR	$[-0.062, +0.091]$	4.0	3.3
RL	$[-0.045, +0.138]$	4.7	2.7
LL+RR	$[-0.012, +0.013]$	9.3	8.6
LR+RL	$[-0.033, +0.096]$	5.5	3.2
$e^+e^- \to f\bar{f}$			
LL	$[-0.010, +0.019]$	10.2	7.3
RR	$[-0.017, +0.026]$	7.7	6.2
VV	$[-0.005, +0.009]$	14.1	10.7
AA	$[-0.006, +0.008]$	13.2	11.0
LR	$[-0.019, +0.042]$	7.3	4.9
RL	$[-0.023, +0.020]$	6.6	7.0
LL+RR	$[-0.006, +0.011]$	12.7	9.5
LR+RL	$[-0.011, +0.013]$	9.8	8.7

Table 6.4:
Results of contact interaction fits to quarks and all fermions based on all LEP2 measurements. The 68% confidence level range is given for ϵ whilst the 95% confidence level limits are given for Λ. The results presented for $f\bar{f}$ assume that the Contact Interaction couples to all the outgoing fermion types with equal strength.

6.2 Limits on TeV-Scale Quantum Gravity

TeV-Scale Quantum Gravity is a recent theory first proposed about two years ago [41, 42]. It approaches the hierarchy problem by introducing extra spatial dimensions of submillimeter size. In contrast to most other models this one does not rely on either SuperSymmetry (SUSY) or Technicolour.

In the following section a short introduction to the ideas behind TeV-Scale Quantum Gravity shall be given. A precise treatment can be found in [42] and a more general introduction to higher dimensional theories in [43]. The analysis carried out and the limits obtained follow a procedure described in [44].

The interaction strength of gravitation is much lower than that of the other three gauge interactions, namely the electromagnetic, the weak and the strong force. The running coupling constants of the latter three interactions are assumed to unify at an energy scale of $\approx 10^{15}GeV$ while the unification with gravity will only occur at the Planck scale of $\approx 10^{19}GeV$. This unification of all the four fundamental forces is described by so called Grand Unified Theories (G.U.T.). One of the most crucial questions the SM cannot answer is why there is such a big discrepancy between the Planck scale and the weak scale ($M_{Planck}/M_{weak} \approx 10^{16}$). This is known as the hierarchy problem.

The behaviour of the gravitational potential as $\sim \frac{1}{r}$ is only proven by direct observation for distances $\geq 1mm$. If one assumes that the gravitational potential rises much more strongly at shorter distances with $\sim \frac{1}{r^n}$, then a unification of gravity with the other forces could take place at a much lower energy scale M_D by using for example string theory. For $M_D \approx M_{weak}$ the hierarchy problem would be solved. For $M_D \gg M_{weak}$ a more conventional solution such as SUSY would be needed to describe physics between the two mass scales.

Generalizing the gravitational potential of a point-like particle from 3 to $3+\delta$ dimensions gives a potential of the form

$$V(r) \approx \frac{1}{r^{1+\delta}} \quad . \tag{6.7}$$

If the extra dimensions are compactified down to a size R, gravity will have the usual $\frac{1}{r}$ dependence for distances $r > R$ while for smaller distances it can propagate in all $3+\delta$ dimensions. The other three forces would remain restricted to the usual three dimensions and therefore the good agreement between the SM and experiments concerning electroweak precision measurements for example, would still remain undisturbed. The relationship between the size of the extra dimensions R, their number δ, the Planck scale M_{Planck} and the scale M_D, where gravity would be of equal strength as the other three forces is

$$\left(\frac{M_{Planck}}{M_D}\right)^2 = 8\pi \left(\frac{RM_D}{\hbar c}\right)^\delta \tag{6.8}$$

where M_{Planck} can be obtained from $M_{Planck} = \sqrt{\frac{\hbar c}{G_N}}$, G_N being the Newtonian gravitational constant.

As an alternative viewpoint one can imagine that the three spatial dimensions are represented by a plane (brane) of infinite size while the extra dimensions δ are represented by a

sphere (bulk) of finite size. Gravity can propagate in all $3+\delta$ dimensions while the remaining three forces are restricted to 3 dimensions in the brane. A massless graviton would then have an energy equal to

$$E^2 = \sum_{i=1}^{3} P_i^2 + \sum_{j=4}^{3+\delta} P_j^2 \tag{6.9}$$

with the P_i being the three components of its momentum. From a limited view-point out of three dimensions one would observe now that $E^2 \neq \sum_{i=1}^{3} P_i$ and the graviton would appear to have a mass

$$M^2 = \sum_{j=4}^{3+\delta} P_j^2 \quad . \tag{6.10}$$

The finite size of the extra dimensions leads to boundary conditions and consequently the momentum components are quantized. Viewed from three dimensions, gravitons will have a discrete mass spectrum. The discrete eigenstates are known as the Kaluza-Klein excitations of the graviton. Nonetheless, this scenario still allows a massless graviton (which has to have zero momentum in the extra dimensions). Massive gravitons give rise for a Yukawa potential and the resulting gravitational potential can be obtained by summing over the contributions of the whole mass spectrum and the massless graviton, which gives

$$V(r) \approx \int_0^\infty \frac{1}{r} e^{-Mr} \rho(M) dM \approx \frac{R^\delta}{r^{1+\delta}} \tag{6.11}$$

with $\rho(M)$ being the number of graviton states per unit mass ($\rho(M) \approx R^\delta M^{\delta-1}$).

It can be seen from eqs. 6.7 and 6.11 that both massless gravitons in $3+\delta$ dimensions and massive gravitons in 3 dimensions lead to a $1/r^{1+\delta}$ dependence of the gravitational potential. In a s-channel exchange of a graviton the whole Kaluza-Klein spectrum is exchanged and as a result this makes up for the smallness of the gravitational coupling constant (as long as $M_D > R$, which is usually the case) to produce an observable effect.

From the Q^2 dependence of the running coupling constants a unification of the electromagnetic, the weak and the strong force is expected at a scale of about 10^{15} GeV. This is in disagreement with the assumption that at a scale $\Lambda \approx M_D$, where gravity becomes strong with $M_D \approx M_{weak}$, gravitation will unify with the other three forces in a G.U.T. theory. In order to avoid this problem, the three dimensional brane is required to extend into the extra dimensions of about M_D. This will cause the gauge bosons to have momentum components in the extra dimensions and in consequence the coupling constants do not run according to the SM prediction so that a unification at a lower energy scale is possible. The parameter Λ represents an ultra-violet cutoff above which a G.U.T. theory has to replace the theory of gravity introduced here.

The differential cross section for graviton exchange predicted by the model described above

and calculated in the Born approximation is given by [45]

$$\begin{aligned}\frac{d\sigma}{dt}(e^+e^- \to f\bar{f}) &= \frac{d\sigma}{dt}(e^+e^- \to f\bar{f})_{SM} \\ &-\frac{N_f\alpha\pi}{2\Lambda^4}\left(Q_eQ_fG_5(t/s) + \frac{1}{\sin^2 2\theta_W}\frac{s}{s-M_Z^2}[v_ev_fG_5(t/s) + a_ea_fG_6(t/s)]\right) \\ &-\frac{\alpha\pi}{2\Lambda^4}\delta_{ef}\left(Q_e^2G_7(t/s) + \frac{1}{\sin^2 2\theta_W}\frac{s}{s-M_Z^2}[v_e^2+a_e^2]G_8(t/s)\right. \\ &\left. + \frac{1}{\sin^2 2\theta_W}\frac{s}{t-M_Z^2}[v_e^2G_9(t/s) + a_e^2G_{10}(t/s)]\right) \\ &+\frac{N_f\pi}{32}\frac{s^2}{\Lambda^8}G_4(t/s) + \frac{\delta_{ef}\pi}{32}\frac{s^2}{\Lambda^8}G_{11}(t/s)\end{aligned} \tag{6.12}$$

where $v_f = I_3 - 2Q_f\sin^2 2\theta_W$, $a_f = I_3$ and $t = (p_{e^-} - p_f)^2$ with I_3 being the third component of the weak isospin. δ_{ef} is equal to 1 for electron pair production ($f = e$) and 0 otherwise. The G_i functions are given in appendix A.2. The interference term of the cross section depends on $1/\Lambda^4$ while the pure graviton exchange terms have a $1/\Lambda^8$ dependence. The deviations from the SM cross section are only very small for all the channels with $f \neq e$ because the interference term vanishes when integrated over all polar angles. The Bhabha channel is the most sensitive to graviton exchange [46] as for this case the interference term between s-channel exchange of a graviton and t-channel exchange of a photon produces a nonvanishing term.

As for the Contact Interactions the deviation from the SM was fitted using eq. 6.2. The contributions to the cross section from the interference term and the pure graviton contribution were calculated in the improved Born approximation. The Born level cross section given in eq. 6.12 was corrected for ISR according to [40]. A maximum likelihood fit was carried out with ϵ being the fit parameter. Like in the previous section a value of $\epsilon = 0$ means that no deviation from the SM is observed. However, the relation between ϵ and Λ is now $\epsilon = 1/\Lambda^4$, having its origin in the different dependence of the cross section on the mass scale Λ. The 68 % confidence level limits on ϵ were obtained in the same way as for the Contact Interactions from eq. 6.4. In addition the central value ϵ^0 was computed as

$$\int_{\epsilon^0}^{\infty}\mathcal{L}(\epsilon')d\epsilon' = 0.5\int_{-\infty}^{\infty}\mathcal{L}(\epsilon')d\epsilon' \quad . \tag{6.13}$$

The 95 % confidence level limits on ϵ were calculated according to eq. 6.5 and transformed to lower limits on Λ with the help of

$$\Lambda_{95}^{\pm} = 1\Big/|\epsilon_{95}^{\pm}|^{1/4} \quad . \tag{6.14}$$

The limit obtained from ϵ_{95}^{-} corresponds to a change in the relative phase between the graviton and SM amplitudes of 180°, which in the absence of a G.U.T. theory is not well predicted.

The results obtained from the different channels and the combined fermion value are presented in table 6.5. As already mentioned, the results are dominated by the Bhabha channel, which in addition shows the smallest deviation from the SM. Furthermore, although all the central values of ϵ differ from zero they are all consistent with zero within the 1 σ range (68 % confidence level).

TeV Scale Quantum Gravity (130 - 202 GeV)

Channel	$\epsilon = 1 / \Lambda^4$ (TeV^{-4})	Λ^-_{95} (TeV)	Λ^+_{95} (TeV)
$q\bar{q}$	$2.80 \pm {}^{3.80}_{4.95}$	0.63	0.58
e^+e^-	$-0.54 \pm {}^{0.55}_{0.53}$	0.91	1.06
$\mu^+\mu^-$	$0.71 \pm {}^{1.97}_{1.97}$	0.73	0.69
$\tau^+\tau^-$	$0.87 \pm {}^{3.14}_{3.24}$	0.64	0.62
$f\bar{f}$	$-0.41 \pm {}^{0.53}_{0.51}$	0.93	1.05

Table 6.5:
Fitted value of $\epsilon = 1/\Lambda^4$ and the 95% confidence level lower limits Λ^+_{95} and Λ^-_{95} obtained using the various difermion channels from 130-202 GeV. The results given for $f\bar{f}$ represent the combination of all channels.

When one assumes that the ultra-violet cut-off parameter Λ is approximately equal to the scale M_D where gravity becomes as strong as the other three gauge interactions, these lower limits on Λ can, for a given number of extra dimensions, be used to obtain an upper limit on the size of the extra dimensions with the help of eq. 6.8. The results are given in table 6.6 but should not be considered to be precise as the approximation made above is just a rough one. Nonetheless, it is an interesting exercise and it becomes apparent that the size of the extra dimensions shrinks rapidly with an increasing number of extra dimensions. Performing this calculation for just one extra dimension would result in an upper limit on the radius of 1×10^{12} m, which is apparently excluded by direct observation.

δ	$R(m)$
1	1×10^{12}
2	4×10^{-4}
3	3×10^{-9}
4	9×10^{-12}
5	3×10^{-13}
6	2×10^{-14}

Table 6.6:
Upper limits on the size of extra dimensions as a function of the number δ of extra dimensions. For $\delta = 1$ the size of the extra dimension $R = 1 \times 10^{12}$ m, which is obviously excluded by direct observation. The limits are derived under the assumption of $M_D \approx \Lambda$, which is only an approximation and should therfore not considered to be precise.

Chapter 7

Conclusions and Comparisons

In this analysis the cross section and forward-backward asymmetry for muon pair production in e^+e^- collisions was measured for centre-of-mass energies of 196, 200 and 202 GeV. The cross section was determined for an inclusive and exclusive sample and the measured values together with statistical and systematic errors are given in table 7.1. Here the numbers for the forward-backward asymmetry determined from the exclusive sample are given as well. As can be seen, the precision of the measurement is dominated by the statistical error. The measured values agree well with SM predictions and no significant deviation is found.

$\sqrt{s'/s}$ cut	E_{CM} (GeV)	ALEPH $\sigma_{\mu\mu}$(pb)	$\sqrt{s'/s}$ cut	OPAL [47] $\sigma_{\mu\mu}$(pb)	SM prediction (pb)
0.1	195.52	$7.57 \pm 0.38 \pm 0.08$	0.1	$7.05 \pm 0.34 \pm 0.25$	7.11
	199.52	$6.83 \pm 0.35 \pm 0.09$		$6.62 \pm 0.33 \pm 0.23$	6.79
	201.63	$6.91 \pm 0.50 \pm 0.09$		$5.63 \pm 0.43 \pm 0.23$	6.63
0.9	195.52	$2.57 \pm 0.18 \pm 0.02$	0.85	$2.90 \pm 0.20 \pm 0.07$	2.46
	199.52	$2.80 \pm 0.18 \pm 0.03$		$2.73 \pm 0.19 \pm 0.08$	2.36
	201.63	$2.49 \pm 0.24 \pm 0.02$		$2.31 \pm 0.26 \pm 0.08$	2.30
$\sqrt{s'/s}$ cut	E_{CM} (GeV)	ALEPH A_{FB}	$\sqrt{s'/s}$ cut	OPAL [47] A_{FB}	SM prediction
0.9	195.52	0.56 ± 0.06	0.85	0.65 ± 0.06	0.57
	199.52	0.43 ± 0.06		0.62 ± 0.06	0.56
	201.63	0.59 ± 0.08		0.48 ± 0.11	0.56

Table 7.1:
Comparison of cross section and A_{FB} measurements by ALEPH and OPAL. Notice the different cuts in $\sqrt{s'/s}$ for the exclusive cross section and forward-backward asymmetry measurement. The SM predictions are given for the ALEPH definitions of $\sigma_{\mu\mu}$ and A_{FB}.

Cross sections and asymmetries are also measured by the other three LEP experiments, OPAL, DELPHI and L3, OPAL being the only one to have released numbers so far [47]. The OPAL results are compared with the results of this analysis[1] in table 7.1.

[1]Here and in the following the results of this analysis are referred to as ALEPH although they are not the official ALEPH results

Model		ALEPH	OPAL [47]	DELPHI [48]	H1 [49]	ZEUS [50]	CDF [51]	DØ [52]
		$e^+e^- f\bar{f}$	$e^+e^- f\bar{f}$	$e^+e^- l^+l^-$	$e^+e^- q\bar{q}$	$e^+e^- q\bar{q}$	$e^+e^- q\bar{q}, \mu^+\mu^- q\bar{q}$	$e^+e^- q\bar{q}$
LL	Λ^- (TeV)	10.2	8.8	7.3	1.3	—	4.3	4.2
	Λ^+ (TeV)	7.3	7.6	9.4	2.4	—	3.1	3.3
RR	Λ^- (TeV)	7.7	8.5	7.4	1.3	—	4.2	4.0
	Λ^+ (TeV)	6.2	7.0	9.0	2.5		3.0	3.3
VV	Λ^- (TeV)	14.1	15.6	13.6	2.8	5.0	6.3	6.1
	Λ^+ (TeV)	10.7	13.4	17.8	5.5	4.7	5.0	4.9
AA	Λ^- (TeV)	13.2	13.3	12.8	3.9	3.7	5.6	5.5
	Λ^+ (TeV)	11.0	12.4	10.2	2.1	2.6	4.5	4.7
LR	Λ^- (TeV)	7.3	8.7	6.4	1.6		3.9	3.6
	Λ^+ (TeV)	4.9	8.1	8.8	3.4		3.3	3.4
RL	Λ^- (TeV)	6.6	9.2	6.4	1.6	—	3.7	3.7
	Λ^+ (TeV)	7.0	8.5	8.8	3.4	—	3.3	3.3
LL+RR	Λ^- (TeV)	12.7	12.1	—	1.4	2.8	—	5.1
	Λ^+ (TeV)	9.5	10.0	—	3.3	2.9	—	4.2
LR+RL	Λ^- (TeV)	9.8	12.5		1.8	4.3		4.4
	Λ^+ (TeV)	8.7	11.7		4.6	4.0		3.9

Table 7.2:
Results of contact interaction fits for various models obtained from different experiments. The 95% confidence level limits are given for Λ. *In the first line the types of Contact Interactions considered for the derivation of the limits are indicated. It is assumed that the Contact Interaction couples to all the outgoing fermion types with equal strength.*

A direct comparison can only be made for the inclusive sample because for the exclusive sample the cut in $\sqrt{s'/s}$ is different ($\sqrt{s'/s} > 0.85$ compared to $\sqrt{s'/s} > 0.9$). Nonetheless, the results should not differ too much as the contribution from the uncommon $\sqrt{s'/s}$ region is small. This can be seen from the $\sqrt{s'/s}$ distribution in figure 5.1 and in fact the results of the two analyses are compatible. In order to obtain greater precision the results of the four LEP experiments can be combined, which will reduce the statistical error by a factor of two, assuming equal integrated luminosities for all the experiments. The correlated systematic errors will decrease as well, e.g. the systematic error on the integrated luminosity while uncorrelated errors will remain unchanged.

From the measurements of the cross sections and angular distributions limits on Contact Interactions were derived. The results obtained from a maximum likelihood fit are comparable to those obtained earlier [31] and are given in table 7.2 for the combined fermion channels. Better limits could be obtained if the theoretical uncertainties would decrease, the most prominent one being ISR/FSR interference. Nonetheless, statistical fluctuations in the data could be a further reason for a stagnation of the limits.

Limits on Contact Interactions are also derived by other experiments at LEP [47, 48], HERA [49, 50] and the Tevatron [51, 52]. Their results are compared with those obtained in this analysis in table 7.2. DELPHI only quotes numbers for the combined leptonic channels while the HERA experiments can only look for $e^+e^-q\bar{q}$ Contact Interactions. D$\emptyset$ quotes limits for the same process while CDF adds a $\mu^+\mu^-q\bar{q}$ Contact Interaction. Combined limits always assume that the Contact Interaction couples to all the outgoing fermion types with equal strength. The LEP results obtained from e^+e^- annihilations are the most stringent (even for the single channels) and are in good agreement with each other. As for the cross section and asymmetries a combination of the results from the four LEP experiments will result in a higher accuracy, especially in the angular distributions, and will most probably lead to higher constraints for Contact Interactions as all the four experiments are in good agreement with the SM predictions.

Finally, limits for TeV-Scale Quantum Gravity were derived, which are summarized in table 7.3. Lower limits for the parameter Λ are given, which is an ultra-violet cut-off parameter representing an energy-scale above which gravity would unify with the other three forces in a G.U.T. theory. Limits are also derived by DELPHI [48] and H1 [49]. While ALEPH uses the full set of data available above the Z resonance, DELPHI only uses the 183-202 GeV data. As HERA is an ep collider the differential cross sections for graviton exchange are obtained by applying crossing relations to the e^+e^- cross sections. All the limits are of the order of 1 TeV, the Bhabha channel in e^+e^- collisions being the most sensitive one as explained in chapter 6.2. The combination of all fermion channels from the fit carried out in this analysis results in a value of $\Lambda^- = 0.93\ TeV$ and $\Lambda^+ = 1.05\ TeV$.

As a conclusion, it can be said that all the measured quantities are well in agreement with the SM. The limits on physics processes beyond the SM are still increasing, even though not as rapidly as before. This could either be due to statistical fluctuations in the data or due to limitations by the errors on the theoretical predictions. Nonetheless, New Physics seems not to be 'around the corner'. The LEP data taking will continue until September 2000,

Channel	$\epsilon = 1 \ / \ \Lambda^4$ (TeV^{-4})	Λ^-_{95} (TeV)	Λ^+_{95} (TeV)
DELPHI [48]			
$\mu^+\mu^-$	$-4.84 \ ^{+\ 2.39}_{-\ 2.02}$	0.59	0.73
$\tau^+\tau^-$	$-4.49 \ ^{+\ 3.46}_{-\ 3.59}$	0.56	0.65
H1 [49]			
$e^+q \to e^+q, \ e^+\bar{q}$	$3.3 \ ^{+\ 4.2\ +\ 0.4}_{-\ 3.3\ -\ 1.3}$	0.72	0.48
ALEPH			
$q\bar{q}$	$2.80 \ ^{+\ 3.80}_{-\ 4.95}$	0.63	0.58
e^+e^-	$-0.54 \ ^{+\ 0.55}_{-\ 0.53}$	0.91	1.06
$\mu^+\mu^-$	$0.71 \ ^{+\ 1.97}_{-\ 1.97}$	0.73	0.69
$\tau^+\tau^-$	$0.87 \ ^{+\ 3.14}_{-\ 3.24}$	0.64	0.62
$f\bar{f}$	$-0.41 \ ^{+\ 0.53}_{-\ 0.51}$	0.93	1.05

Table 7.3:
Fitted value of $\epsilon = 1 \ / \Lambda^4$ and the 95% confidence level lower limits Λ^+_{95} and Λ^-_{95} for various difermion channels. For the ALEPH limits data from 130-202 GeV was used as input while DELPHI only used the 183-202 GeV data. The limits derived from H1 are calculated by applying crossing relations to the e^+e^- cross section.

collecting data at centre-of-mass energies $\geq$ 205 *GeV*, presumably about 150 pb^{-1}. With this additional data the predictions of the SM can be tested at higher centre-of-mass energies than it has been done in this analysis and the limits for processes beyond the SM can be pushed higher, provided no unexpected phenomena appear.

Appendix A

Formulae and Functions for New Physics

A.1 Born level differential cross section for Contact Interactions

Born level differential cross section for e^+s^- annihilation including interference effects between Contact Interactions and the SM Born processes [39]:

$$\begin{aligned}\frac{4s}{\alpha^2}\frac{d\sigma}{d\Omega}(e^+e^- \to f\bar{f}) = & \left[|\tilde{\mathcal{A}}^{ee}_{LR}(t)|^2 + |\tilde{\mathcal{A}}^{ee}_{RL}(t)|^2\right]\left(\frac{s}{t}\right)^2\delta_{ef} \\ + & \left[|\mathcal{A}^{ef}_{LR}(s)|^2 + |\mathcal{A}^{ef}_{RL}(s)|^2\right]\left(\frac{t}{s}\right)^2 \\ + & \left[|\mathcal{A}^{ef}_{LL}(s)|^2 + |\mathcal{A}^{ef}_{RR}(s)|^2\right]\left(\frac{u}{s}\right)^2 \quad ,\end{aligned} \tag{A.1}$$

where $s = 4E^2_{beam}$, $t = -\frac{1}{2}s(1-\cos\theta)$ and $s+t+u=0$.

The helicity amplitudes $\mathcal{A}^{ef}_{ij}$ used in the differential cross section are defined as:

$$\tilde{\mathcal{A}}^{ee}_{ij}(t) = Q_e^2 + c^e_i c^e_j \tilde{\chi}(t) + \eta_{ij}\frac{t}{\alpha}\frac{1}{\Lambda^2} \qquad (i \neq j) \tag{A.2}$$

$$\mathcal{A}^{ef}_{ij}(s) = Q_e Q_f + c^e_i c^f_j \chi(s) + \eta_{ij}\frac{s}{\alpha}\frac{1}{\Lambda^2} \qquad (i \neq j) \tag{A.3}$$

$$\mathcal{A}^{ef}_{ij}(s) = Q_e Q_f + c^e_i c^f_j\left[\chi(s) + \tfrac{s}{t}\tilde{\chi}(t)\delta_{ef}\right] \tag{A.4}$$

$$+\tfrac{s}{t}\delta_{ef} + (1+\delta_{ef})\eta_{ij}\tfrac{s}{\alpha}\tfrac{1}{\Lambda^2} \qquad (i = j) \tag{A.5}$$

The parameters $c^f_{L,R}$ are the left- and right-handed couplings of the fermions to the Z-boson. The Z propagators $\chi(s) = Cs/(s - M_Z^2 + iM_Z\Gamma_Z)$ and $\tilde{\chi}(t) = Ct/(t - M_Z^2)$ in the s and t channels contain a factor C which depends on the renormalization scheme chosen.

A.2 The $G_i(x)$ functions for TeV Scale Quantum Gravity

The $G_i(x)$ functions used in eq. 6.12 for the definition of the differential cross section as defined in [45] are:

$$G_4(x) = 1 + 10x + 42x^2 + 64x^3 + 32x^4 \quad \text{(A.6)}$$

$$G_5(x) = 1 + 6x + 12x^2 + 8x^3 \quad \text{(A.7)}$$

$$G_6(x) = 1 + 6x + 6x^2 \quad \text{(A.8)}$$

$$G_7(x) = 9x^{-1} + 22 + 24x + 11x^2 + x^3 \quad \text{(A.9)}$$

$$G_8(x) = 4 + 9x + 6x^2 + x^3 \quad \text{(A.10)}$$

$$G_9(x) = 9 + 18x + 15x^2 + 5x^3 \quad \text{(A.11)}$$

$$G_{10}(x) = 1 + 12x + 15x^2 + 5x^3 \quad \text{(A.12)}$$

$$G_{11}(x) = 40 + 114x + 126x^2 + 60x^3 + 9x^4 \quad \text{(A.13)}$$

Bibliography

[1] S. S. Schweber, *QED and the men who made it: Dyson, Feynman, Schwinger, and Tomonaga* , Princeton, USA: University Press (1994) 732 p.

[2] P. W. Higgs, Phys. Lett. **12**, 132 (1964).

[3] P. W. Higgs, Phys. Rev. Lett. **13**, 508 (1964).

[4] P. W. Higgs, Phys. Rev. Lett. **145**, 1156 (1966).

[5] S. L. Glashow, Nucl. Phys. **22**, 579 (1961).

[6] A. Salam, in *Elementary Particle Theory*, ed. N. Svartholm, Proceedings of the Nobel Symposium held 1968 at Lerum, Sweden, Stockholm 1968, 367-377.

[7] S. Weinberg, Phys. Rev. Lett. **19**, 1264 (1967).

[8] G. Arnison et al., UA1 Collaboration, Phys. Lett. **B122**, 103 (1983).

[9] G. Arnison et al., UA1 Collaboration, Phys. Lett. **B126**, 398 (1983).

[10] M. Banner et al., UA2 Collaboration, Phys. Lett. **B122**, 476 (1983).

[11] P. Bagnaia et al., UA2 Collaboration, Phys. Lett. **B129**, 130 (1983).

[12] F. Halzen and A. D. Martin, *Quarks and leptons: An introductory course in modern particle physics* , New York, USA: Wiley (1984) 396 p.

[13] O. Nachtmann, *Elementary particle physics: Concepts and phenomena* , Berlin, Germany: Springer (1990) 559 p.

[14] D. H. Perkins, *Introduction to high-energy physics* , Reading, USA: Addison-Wesley (1982) 437 p.

[15] D. Bardin *et al.*, (1999), hep-ph/9908433.

[16] M. Consoli, W. Hollik and F. Jegerlehner, presented at Workshop on Z Physics at LEP.

[17] C. Caso *et al.*, Eur. Phys. J. **C3**, 1 (1998).

[18] F. Eisele, Summary talk given at the XXXV Rencontres de Moriond, Les Arcs, March 11-18 2000.

[19] S. Myers et al., *Large electron-positron storage ring* , Technical Notebook, CERN (1988).

[20] C. Bowdery (Editor), *ALEPH handbook, Vol. 1 & 2* , CERN (1997).

[21] ALEPH, D. Buskulic *et al.*, Nucl. Instrum. Meth. **A360**, 481 (1995).

[22] ALEPH, R. Barate *et al.*, Eur. Phys. J. **C12**, 183 (2000).

[23] E. Merle, *Mesures des sections efficaces et des asymetries difermioniques avec le detecteur ALEPH a LEP2 - Interpretations au-dela du Modele Standard*, PhD thesis, Laboratoire d'Annecy-le-vieux de Physique des Particules, 1999.

[24] H. Albrecht, E. Blucher and J. Boucrot, ALEPH 99-087.

[25] ALEPH, D. Buskulic *et al.*, Phys. Lett. **B313**, 509 (1993).

[26] S. Jadach, W. Placzek and B. F. L. Ward, Phys. Lett. **B390**, 298 (1997).

[27] T. Sjostrand, Computer Phys. Comm. **82**, 74 (1994).

[28] S. Jadach, B. F. L. Ward and Z. Was, Computer Phys. Comm. **79**, 503 (1994).

[29] M. Skrzypek, S. Jadach, W. Placzek, and Z. Was, Computer Phys. Comm. **94**, 216 (1996).

[30] B. Bloch-Devaux and P. H. Hansen, internal note, ALEPH NOTE 2000-003.

[31] The ALEPH Collaboration, ALEPH CONF 99-013, ALEPH contribution to the Winter Conferences 1999.

[32] The ALEPH Collaboration, ALEPH CONF 2000-021, ALEPH contribution to the Winter Conferences 2000.

[33] ALEPH, R. Barate *et al.*, Eur. Phys. J. **C14**, 1 (2000).

[34] ALEPH, R. Barate *et al.*, Phys. Lett. **B469**, 287 (1999).

[35] D. Bardin *et al.*, Computer Phys. Comm. **104**, 161 (1997).

[36] ALEPH, R. Barate *et al.*, hep-ex/0005043, to be published in Phys. Lett.

[37] H. Harari and N. Seiberg, Phys. Lett. **B98**, 269 (1981).

[38] E. Eichten, K. Lane and M. E. Peskin, Phys. Rev. Lett. **50**, 811 (1983).

[39] H. Kroha, Phys. Rev. **D46**, 58 (1992).

[40] M. Martinez, L. Garrido, R. Miquel, J. L. Harton, and R. Tanaka, Z. Phys. **C49**, 645 (1991).

[41] N. Arkani-Hamed, S. Dimopoulos and G. Dvali, Phys. Lett. **B429**, 263 (1998).

[42] N. Arkani-Hamed, S. Dimopoulos and G. Dvali, Phys. Rev. **D59**, 086004 (1999).

[43] P. D. B. Collins, A. D. Martin and E. J. Squires, *Particle physics and cosmology* , New York, USA: Wiley (1989) 496p.

[44] I. Tomalin, internal note, ALEPH NOTE 99-036.

[45] G. F. Giudice, R. Rattazzi and J. D. Wells, Nucl. Phys. **B544**, 3 (1999).

[46] T. G. Rizzo, SLAC-PUB-8036 (1998).

[47] The OPAL Collaboration, OPAL NOTE PN424.

[48] DELPHI Collaboration, DELPHI 2000-036, DELPHI contribution to the Winter Conferences 2000.

[49] H1, C. Adloff *et al.*, Phys. Lett. **B479**, 358 (2000).

[50] ZEUS, J. Breitweg *et al.*, Eur. Phys. J. **C14**, 239 (2000).

[51] CDF, F. Abe *et al.*, Phys. Rev. Lett. **79**, 2198 (1997).

[52] D0, B. Abbott *et al.*, Phys. Rev. Lett. **82**, 4769 (1999).

Danksagung

Zunächst möchte ich mich bei Herrn Prof. Dr. A. Putzer bedanken, der mir die Durchführung dieser Arbeit innerhalb der ALEPH Gruppe ermöglichte, die Betreuung dieser Arbeit übernahm und durch sein stetes Interesse wesentlich zum Gelingen derselben beitrug. Desweiteren möchte ich Herrn Dr. W.-D. Schlatter danken, der mir die Möglichkeit eines halbjährigen Aufenthaltes am CERN eröffnete.

Herrn Prof. Dr. E.-E. Kluge danke ich für seine Tätigkeit als Zweitgutachter.

Ein ganz besonderer Dank gilt Herrn Dr. C. Geweniger, der die Betreuung meiner Arbeit am CERN übernahm, für gelegentlich stundenlange Diskussionen über elektroschwache Physik (*"Oh je, schon wieder so spät?"*), sein herzliches Lachen und viele Unterhaltungen jenseits der Physik. Gleiches gilt auch für Herrn Dr. S. Dhamotharan, der mir zusätzlich ersteinmal den Umgang mit Computern beibringen mußte und der es schaffte mich zur rechten Zeit von denselben auch wieder loszueisen (*"...serious boozing!"*).

Desweiteren möchte ich mich bei den Mitgliedern der ALEPH Gruppen am Kirchhoff-Institut für Physik in Heidelberg und am CERN für die freundliche Aufnahme und die zahlreichen Hilfestellungen bedanken. Hierbei möchte ich besonders Herrn Dr. R. Cavanaugh für seine Kommentare und Anregungen zu dieser Diplomarbeit danken. Nicht zu vergessen natürlich auch die H1 Gruppe, die immer tapfer die Mensa mitertrug.

Für seinen verzweifelten Versuch mir die englischen Kommaregeln beizubringen und den Hinweis, daß man *"where"* nicht im Sinne von *"wobei"* benutzen kann danke ich Harry, der zusammen mit Selvam und Wouter das Korrekturlesen dieser Arbeit übernommen hatte.

Zu guter letzt seien die Angestellten des Kirchhoff-Institutes (besonders die Kaffeerunde) nicht vergessen, die ja schliesslich für die sehr freundliche und gute Atmosphäre innerhalb des Institutes sorgen. Ich hatte eine schöne Zeit während der Diplomarbeit und ebenso viel Spaß.

Mein tiefster Dank gilt meinen Eltern für Ihre Unterstützung während des Studiums.

Erklärung:

Ich versichere, dass ich diese Arbeit selbständig verfasst und keine anderen als die angegebenen Quellen und Hilfsmittel benutzt habe.

Heidelberg, den .....

.....
(Unterschrift)